ELSEVIER

Contents lists available at ScienceDirect

# Results in Engineering

journal homepage: www.sciencedirect.com/journal/results-in-engineering



# Contour Analysis for Heat Transfer Rate in a Wedge Geometry with Non-Uniform Shapes Nanofluid: Gradient Descent Machine Learning Technique

S. Suresh Kumar Raju <sup>a</sup>, P Durgaprasad <sup>b</sup>, José Luis Díaz Palencia <sup>c</sup>, Abderrahim Wakif <sup>d</sup>, C.S.K. Raju <sup>e</sup>, Maddina Dinesh kumar <sup>c,f,\*</sup>, Muneerah Al Nuwairan <sup>a</sup>, Ali J.Chamkha <sup>g</sup>

- <sup>a</sup> Department of Mathematics and Statistics, College of Science, King Faisal University, Al-Ahsa, 31982, Saudi Arabia
- <sup>b</sup> Department of Mathematics, SAS, Vellore Institute of Technology, Chennai, 600127, India
- <sup>c</sup> Department of Mathematics and Education, Universidad a Distancia de Madrid 28400, Madrid, Spain
- <sup>d</sup> Laboratory of Mechanics, Faculty of Sciences Ain Chock, Hassan II University, Casablanca, 5366, Maarif, Morocco
- e RTA Centre for Science Innovation, School of Computer Science and Engineering, RV University, Bangalore, India
- f Department of Mathematics, B V Raju Institute of Technology, Narsapur, Medak, Telangana, 502313, India
- g Faculty of Engineering, Kuwait College of Science and Technology, Doha District, 35004 Kuwait

### ARTICLE INFO

Keywords: Unsteady flow Wedge Ternary nanofluid, Contour plots analysis Inclination angle Machine learning

### ABSTRACT

The flow of boundary layer over porous wedge nanofluids, hybrid nanofluids, and ternary hybrid nanofluids under constant transverse magnetic field and heat radiation have all been examined. The following cases are taken into consideration: Zirconium oxide + A A7072 + Polyethylene Glycol-water (Case-2); Magnesium oxide + Polyethylene Glycol-water + AA7072 + Zirconium oxide (Case-3); Polyethylene-water as base fluid; nanofluid, hybrid nanofluid, ternary hybrid nanofluid cases. The governing equations are solved using the shooting technique with the fourth-order Runge-Kutta method. The approximate relationship between temperature, velocity, heat transfer rate, and friction factor coefficient at the wedge is shown graphically for a range of values of the pertinent parameters. The flow of boundary layer over porous wedge nanofluids, hybrid nanofluids, and ternary hybrid nanofluids under constant transverse magnetic field and heat radiation have all been examined. Cases  $containing\ Polyethylene\ Glycol-Water\ +\ AA7072\ (Case-1),\ Zirconium\ oxide\ +\ A\ A7072\ +\ Polyethylene\ Glycol-Water\ +\ AA7072\ (Case-1),\ Zirconium\ oxide\ +\ A\ A7072\ +\ Polyethylene\ Glycol-Water\ +\ AA7072\ (Case-1),\ Zirconium\ oxide\ +\ A\ A7072\ +\ Polyethylene\ Glycol-Water\ +\ AA7072\ (Case-1),\ Zirconium\ oxide\ +\ A\ A7072\ +\ Polyethylene\ Glycol-Water\ +\ AA7072\ (Case-1),\ Zirconium\ oxide\ +\ A\ A7072\ +\ Polyethylene\ Glycol-Water\ +\ AA7072\ (Case-1),\ Zirconium\ oxide\ +\ A\ A7072\ +\ Polyethylene\ Glycol-Water\ +\ AA7072\ (Case-1),\ Zirconium\ oxide\ +\ A\ A7072\ +\ Polyethylene\ Glycol-Water\ +\ AA7072\ (Case-1),\ Zirconium\ oxide\ +\ A\ A7072\ +\ Polyethylene\ Glycol-Water\ +\ AA7072\ (Case-1),\ Zirconium\ oxide\ +\ A\ A7072\ +\ Polyethylene\ Glycol-Water\ +\ AA7072\ (Case-1),\ Zirconium\ oxide\ +\ AA707$ water (Case-2), and Magnesium oxide + Polyethylene Glycol-water + AA7072 + Zirconium oxide (Case-3) are taken into consideration. Polyethylene water is used as the base fluid. The governing equations are solved using the shooting approach and Runge-Kutta fourth order. The approximate relationship between temperature, velocity, heat transfer rate, and friction factor coefficient at the wedge is shown graphically for a range of values of the pertinent parameters. Comparing Ternary hybrid nanofluid to nanofluid and hybrid nanofluid situations, it is discovered that the skin friction coefficient is higher. It has also been noted that ternary hybrid nanofluids have a higher Nusselt number than hybrid and nanofluids. When applied to specific dimensionless parameters, the basic linear regression machine learning technique using the gradient descent method accurately predicts the truth values. Finding the optimisation conditions values based on the key factors influencing the Response Function is easier with the RSM method's help. When applied to specific dimensionless parameters, simple linear regression machine learning using the gradient descent method accurately predicts the truth values.

# 1. Introduction

The broad range of practical uses and widespread adoption of

magnetohydrodynamics (MHD) generate curiosity in investigating new research projects in various flow situations and shapes using distinct numerical techniques. Magnetohydrodynamics, introduced by Hannes

<sup>\*</sup> Corresponding author. Department of Mathematics and Education, Universidad a Distancia de Madrid 28400, Madrid, Spain.

E-mail addresses: ssurapuraju@kfu.edu.sa (S.S.K. Raju), durgaprasad.p@vit.ac.in (P. Durgaprasad), joseluis.diaz.p@udima.es (J.L. Díaz Palencia), wakif.

abderrahim@gmail.com (A. Wakif), sivapdf90@gmail.com (C.S.K. Raju), dineshmaddina319@gmail.com (M. Dinesh kumar), msalnuwairan@kfu.edu.sa (A.N. Muneerah), achamkha@gmail.com (J.Chamkha Ali).

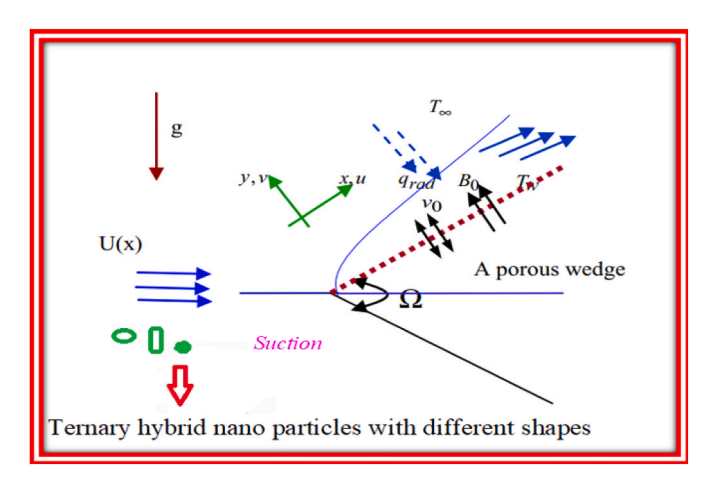
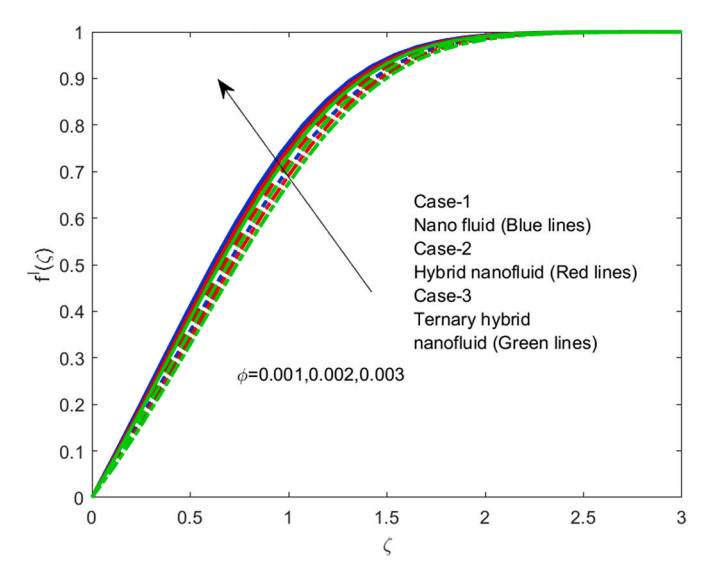


Fig:1. Flow geometry.

Alfvén, studies conductive fluid motion, earning him the 1970 Nobel Prize. It finds diverse applications in metallurgy and manufacturing, including flow measurement, power generation, pumping, and nuclear reactors. Boundary layer flow analysis over wedges is receiving considerable fluid mechanics because of its several uses in thermal engineering. Falkner and Skan [1] investigated a wedge's fluid flow using the Prandtl boundary layer concept, which has influenced recent progress in wedge applications. Ibrahim and Tulu [2] investigated the mass and heat transfer that happens when a boundary layer passes over a wedge, when magnetohydrodynamics (MHD) is present; using various factors, they noted changes in the thermal boundary layer. Mishra and Kumar [3] extensively investigated the magnetohydrodynamic (MHD) flow across a wedge. Nevertheless, Hussain et al. [4] examined how suction and blowing affect a Williamson fluid's magnetohydrodynamics (MHD) passing over a stretching porous wedge. They observed the variations in heat generation and absorption effects based on different parameters.

Choi [5] presented the concept of "nanofluids," which are specific mixtures of a base fluid and nanoparticles in a colloidal suspension. These nanoparticles demonstrate thermal conductivities significantly higher than the base fluids, usually with diameters less than 100 nm. Researchers enhanced the fluid's quality by adding two or three nanomaterials or nanoparticles to the base fluid after conducting an in-depth investigation and study on the characteristics of nanofluids. This resulted in the creation of hybrid and ternary hybrid nanofluids. A wide range of experts are currently studying the distinct properties of these three fluids to enhance various industrial and medical applications. Adnan and Wagas [6] evaluated the thermal storage of hybrid and ternary hybrid nanofluids in a constant magnetic field, concluding that trihybrid nanofluids are superior for heat storage and purification purposes. Bilal et al. [7] analysed Darcy ternary hybrid nanofluid flow over various geometries, noting more excellent velocity rates over cones than wedges and plates for multiple parameters. They observed that the velocity and energy propagation rates were higher over a cone surface than a wedge and plate as the Grashof number, porosity effect, and heat source changed. Zainal et al. [8] investigated how magnetic fields affect the hybrid nanofluid moving around a wedge that is either stretching/shrinking. The researchers acquired the theoretical findings and

verified that the ternary hybrid nano-fluid exhibits superior dynamic characteristics compared to the hybrid nano-fluid. Also, they confirmed the effectiveness of the Daftardar-Jafari Method (DJM) technique in terms of efficiency. Kezzar et al. [9] research shows that magnetic fields stabilise ternary hybrid nanofluid flow while increasing velocity and boundary friction. According to the results, hybrid nanofluids are thought to have better thermal efficiency than ordinary fluids. The increase in magnetic properties contributes about 12.3 % and 18.8 %, respectively, to the heat transfer rate. Amar [10] discussed the viscous dissipation and heat transfer effect on MHD boundary layer flow past a wedge of nano fluid embedded in a porous media.



**Fig:2.** The result of  $\varphi$  on  $f'(\zeta)$ .

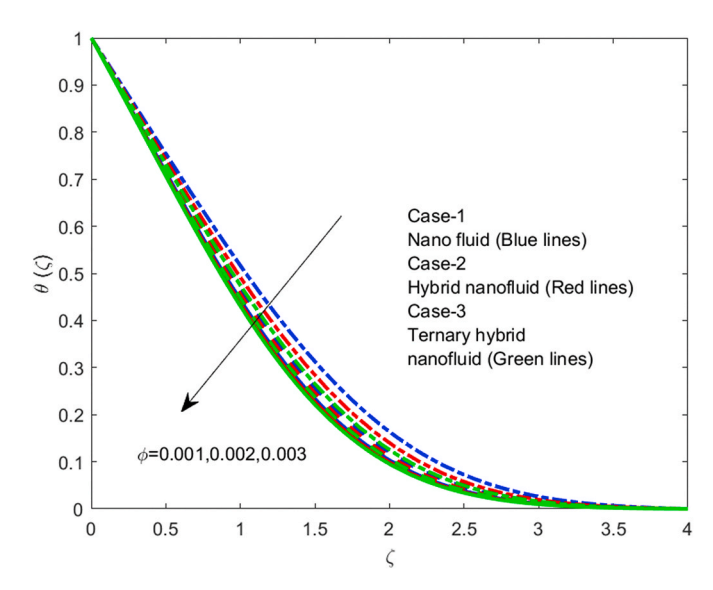


**Fig:3.** The result of  $\varphi$  on  $\theta(\zeta)$ .

**Table 1**Thermophysical properties of Ternary hybrid nanofluid, Nanoparticles with different nanoparticle shapes.

	Nomenclature of nano-particles and base fluid	$\binom{ ho}{\left(kg/m^3 ight)}$	$C_p \ (J/kgK)$	<i>K</i> ( <i>W/mK</i> )	Nano particles shapes
Base fluid	Polyethylene Glycol-Water	1110	3354	0.3712	
Ternary hybrid Nanofluid	AA7072	2720	893	222	Spherical
	Zirconium oxide	5680	502	1.7	Cylindrical
	Magnesium oxide	3560	955	45	Platelet

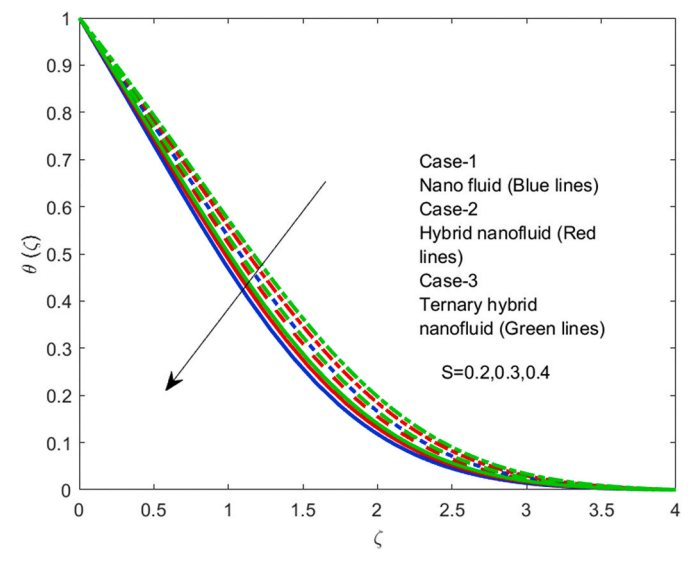


**Fig:4.** The result of *S* on  $\theta(\zeta)$ .

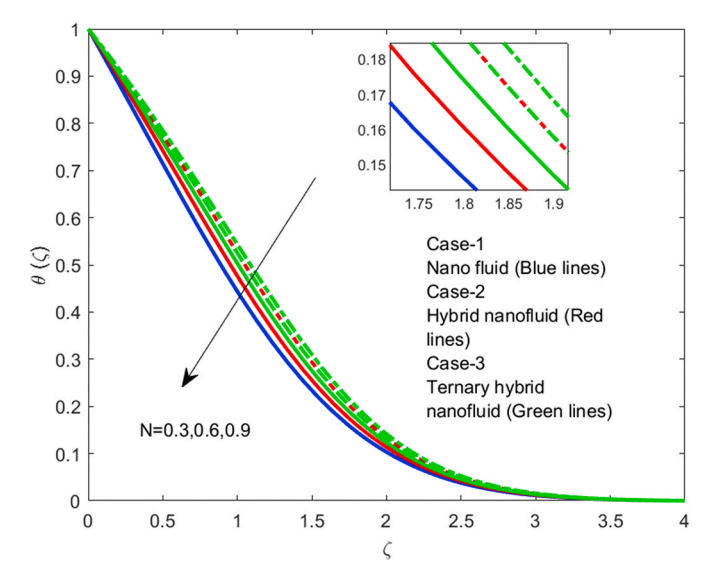


**Fig:6.** The result of *N* on  $\theta(\zeta)$ .

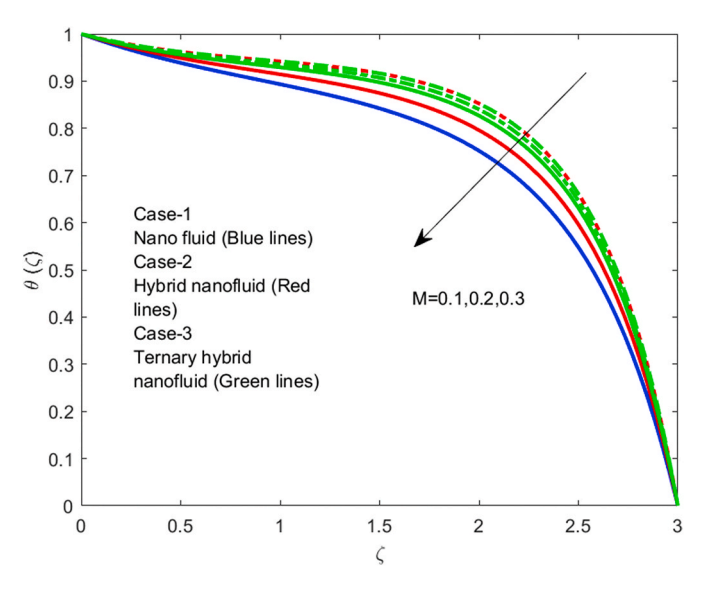


**Fig:5.** The result of M on  $\theta(\zeta)$ .

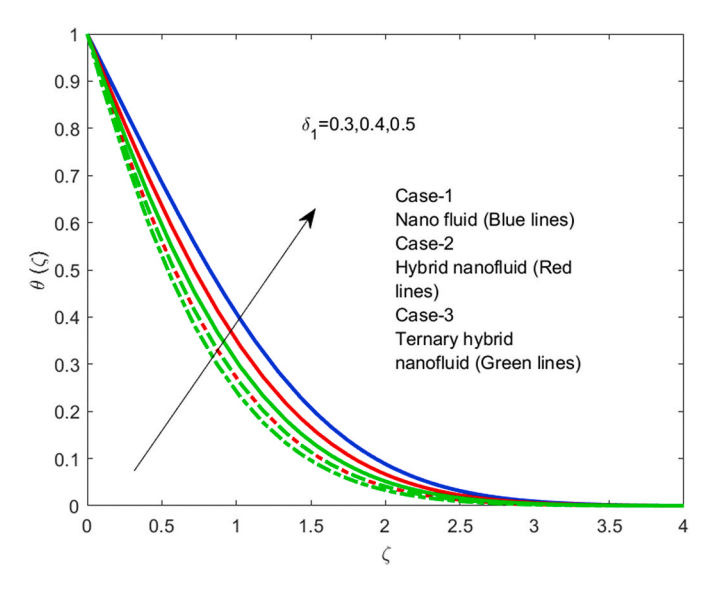


**Fig:7.** The result of  $\delta_1$  on  $\theta(\zeta)$ .

A porous medium refers to a natural or manufactured substance that contains empty spaces filled with gases or liquids. Porous mediums, such as rocks, soil, bones, wood, and cement, are frequently observed in various fields, including biology, material science, and geosciences. Rashid Ahmad and Waqar Ahmed Khan [11] discussed the effect of viscous dissipation and internal heat generation/absorption on heat transfer flow over a moving wedge with convective boundary conditions. The researchers concluded that when a heat source is present, a high value of the convection parameter results in high dimensionless temperature and its gradients in thermal boundary layers. In the presence of radiation and temperature stratification, Nath et al. [12] investigated a numerical analysis on the MHD ternary hybrid nanofluid (Cu + Al2O3+TiO2/H2O) over a vertically stretched cylinder in a porous media. It can be observed that the ternary hybrid nanofluid exhibits a greater heat transfer rate compared to both hybrid and conventional nanofluids. Das et al. further explained the impact of the nanoparticle shape factor on radiative ternary hybrid nanofluid flow over a wedge in the presence of an induced magnetic field [13]. This study explores the hydrothermal transformations of radiative water-based ternary hybrid nanofluidic transport beyond a stationary

and moving wedge while exposed to solar radiation-induced heating and magnetic fields. This work has taken into account the form of the nanoparticles. Hamza et al. [14] reported on MHD radiative Gr-Ag-TiO2/H2O ternary hybrid nanofluid flow on a permeable movable wedge with irreversibility analysis. They concluded that. The ternary hybrid nanofluid, shown to accelerate heat transmission by 6.55 % compared to an ordinary fluid, has the maximum Nusselt number. The effect of nanoparticle shape on improving the heat transfer of magnetised ternary hybrid nanofluid has been studied by Shanmugapriya et al. [15]. Carbon nanotubes, characterised by their distinctive tubular structure, exhibit significant potential in diverse areas. These tiny cylindrical structures, classified as either single-walled or multi-walled, possess a broad range of uses in industries and the field of biomedicine. In fluid dynamics, researchers such as Ding et al. [16] investigated the unique ability to control heat flow in fluids.

Thermal radiation is essential for the movement of fluids and the transfer of heat. It is a fundamental attribute of any material system at temperatures above absolute zero. It is necessary to promote heat transmission in machinery operating at high temperatures. The influence of natural convection is of the utmost significance in various

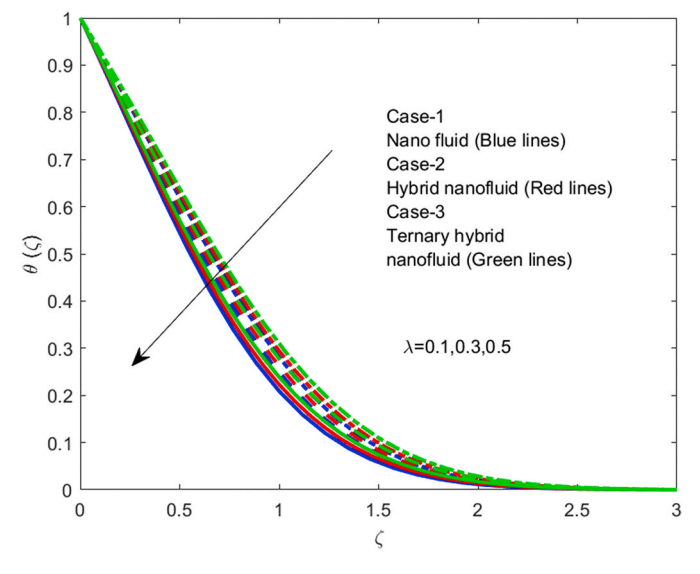


**Fig:8.** The result of  $\lambda$  on  $\theta(\zeta)$ .

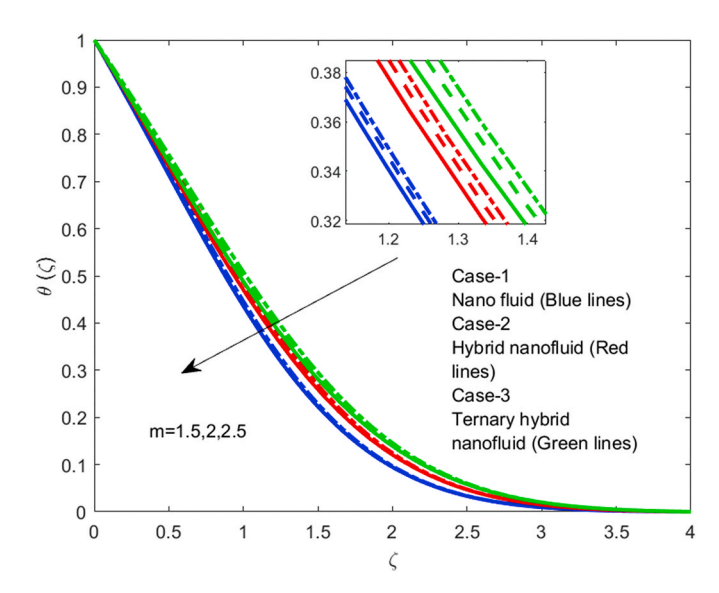


**Fig:10.** The result of *m* on  $\theta(\zeta)$ .

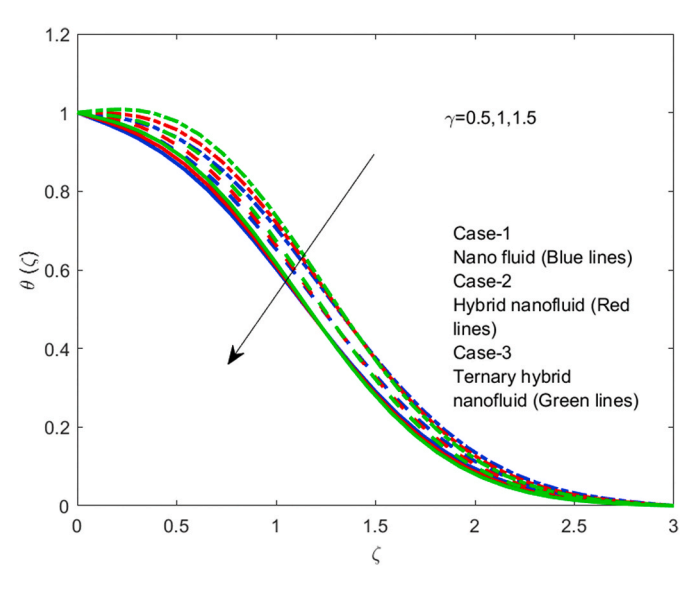


**Fig:9.** The result of  $\gamma$  on  $\theta(\zeta)$ .

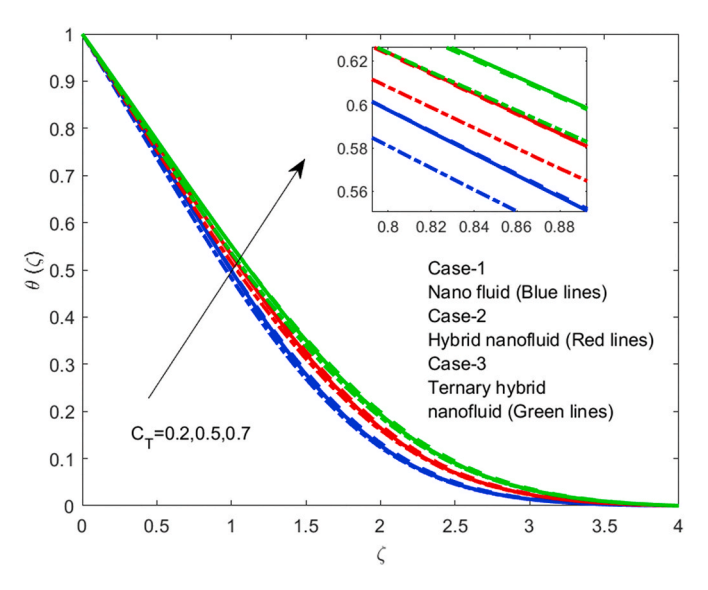


**Fig:11.** The result of  $C_T$  on  $\theta(\zeta)$ .

domains, including physics, engineering, space technology, and gas turbines. In their study, Berrehal and Maougal [17] investigated the entropy-generation phenomenon that occurs when MWCNT nanofluid flows over a wedge. Kandasamy et al. [18] examined single-walled carbon nanotubes on MHD unsteady flow over a porous wedge with heat radiation and changeable stream conditions. They concluded that SWCNTs-water's momentum and thermal boundary layer thickness exhibit greater strength than Cu-water in the presence of uniform thermal radiation as the magnetic field increases. The computational insights into form effects and heat transport enhancement in MHD-free convection of polar ternary hybrid nanofluid around a radiant sphere were investigated by El-Sayed et al. [19]. They observed that the increasing fluid velocity and thermal performance largely depend on the volume fraction and thermal radiation parameters. The magnetic and micropolar effects strongly suppress fluid velocity and energy transfer. The thin-film flow of a ternary hybrid nanofluid over a spinning disc under the influence of a magnetic field resulting from nonlinear convection has been studied by Ullah et al. [20]. The results showed that ternary hybrid nanofluids are more effective at enhancing the thermal performance of conventional fluids than nanofluids. The heat transfer

study of MHD water-modified carbon nanotube flow over a static/moving wedge was performed by Khan et al. [21]. Evidence demonstrates that the magnetic field diminishes the thickness of the boundary layer while augmenting skin friction and Nusselt numbers. Due to their greater density and thermal conductivity, SWCNTs exhibit increased skin friction and Nusselt numbers. The study of MHD natural convection in 2D and 3D cavities with thermal radiation effects has been examined by Zhang et al. [22]. They observed that thermal radiation enhances the flow and heat transfer in the z-direction within the 3D cavity, but the magnetic field has the opposite effect.

This study examines the heat transfer rates in a wedge-shaped structure, considering the impact of non-linear thermal radiation through a porous medium. Additionally, the accuracy of the findings will be validated using the gradient descent machine learning method. The study aims to construct a mathematical model that accurately describes the many mechanisms involved in heat transfer. It will also develop contour maps to represent the visual distribution of heat. Furthermore, it will evaluate the influence of non-linear thermal radiation on the heat transfer rates within the designated geometry and medium. The findings intend to validate the accuracy of expected and

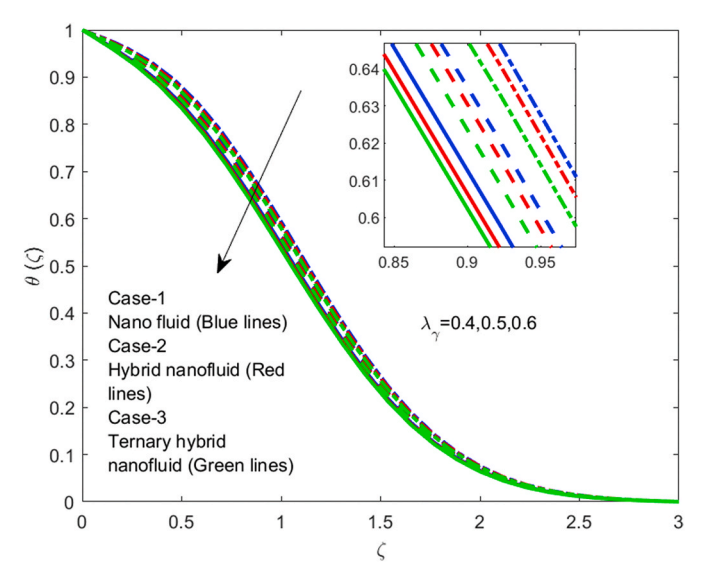


**Fig:12.** The result of  $\lambda_{\gamma}$  on  $\theta(\zeta)$ .

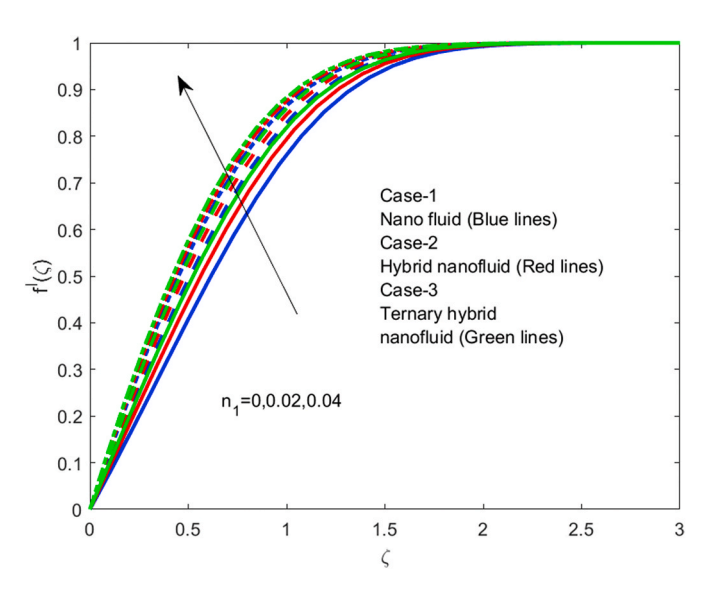
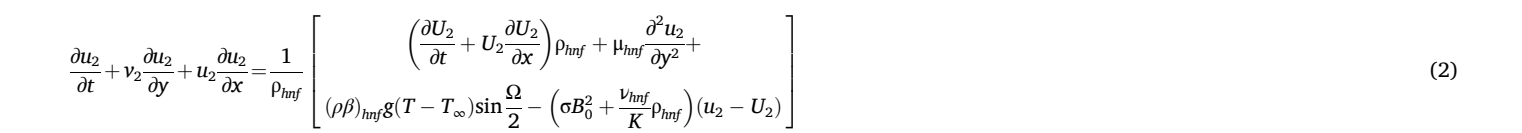


**Fig:13.** The result of  $n_1$  on  $f'(\zeta)$ .

actual values and explore optimisations in heat transfer efficiency by employing the gradient descent method. The results are anticipated to have substantial significance for engineering and materials science applications in which effective heat transport in complex forms is essential.

### 2. Mathematical formulation



Consider a two-dimensional unstable boundary layer involving magnetohydrodynamics. The figure labelled as Fig. 1 shows the Darcy flow of an incompressible viscous ternary hybrid nanofluid (consisting of AA7072, Zirconium Oxide, and Magnesium Oxide mixed with

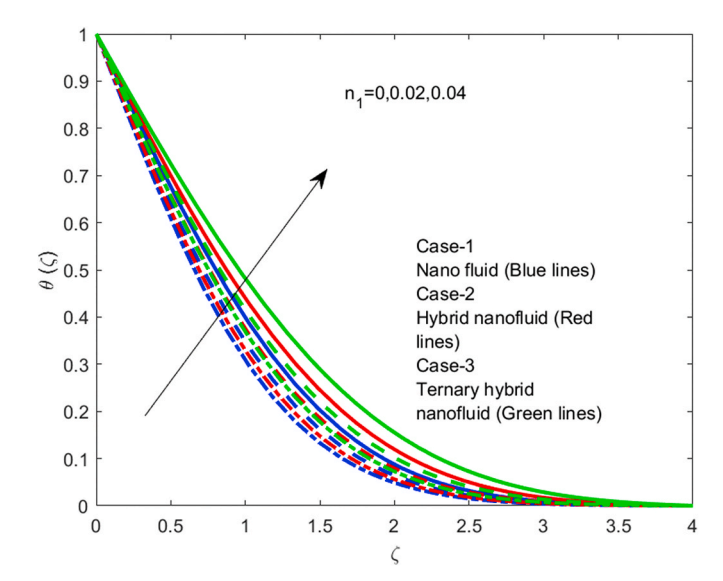


**Fig:14.** The result of  $n_1$  on  $\theta(\zeta)$ .

Polyethylene and water) over a porous wedge sheet. The flow conditions vary throughout the flow. The temperature at the wedge sheet  $(T_w)$ , and the ambient temperature  $(T_\infty)$  Remain constant,. In contrast, the magnetic strength  $(B_0)$  is applied parallel to the y- axis. The ternary hybrid nanofluid is a mixture of polyethene, water, AA7072, zirconium oxide, and magnesium oxide. It is presumed that the base fluids (polyethylenewater) and the suspended ternary hybrid nanoparticles are in a state of thermal equilibrium. Table 1 displays the thermophysical characteristics of the nanofluids.

- It is assumed that the porous wedge is transparent and in thermal equilibrium with the ternary hybrid nanofluids.
- A non-reflecting, absorbing, preferably transparent wedge sheet can measure the intensity of incident radiation flux, denoted as  $q''_{rad}$ .
- The thermal radiation flow passes through the plate and is absorbed by a neighbouring fluid with an absorption coefficient.
- The magnetic field generated by the fluid motion is denoted as \( \overline{B} \),
   While the impact of fluid polarisation is considered to be minor and represented as \( \overline{E} \).

Based on the assumptions stated earlier, the governing system of non-linear partial differential equations that comprises continuity, momentum, and energy equations (Kandaswamy et al. [23] and Kandasamy et al. [28]) can be described as:

$$\frac{\partial v_2}{\partial y} + \frac{\partial u_2}{\partial x} = 0 \tag{1}$$

$$\frac{\partial T}{\partial t} + u_2 \frac{\partial T}{\partial x} + v_2 \frac{\partial T}{\partial y} = \frac{1}{\left(\rho c_p\right)_{hnf}} \left( k_{hnf} \frac{\partial^2 T}{\partial y^2} - \frac{\partial q_r''}{\partial y} - Q_0 (T - T_\infty) \right)$$
(3)

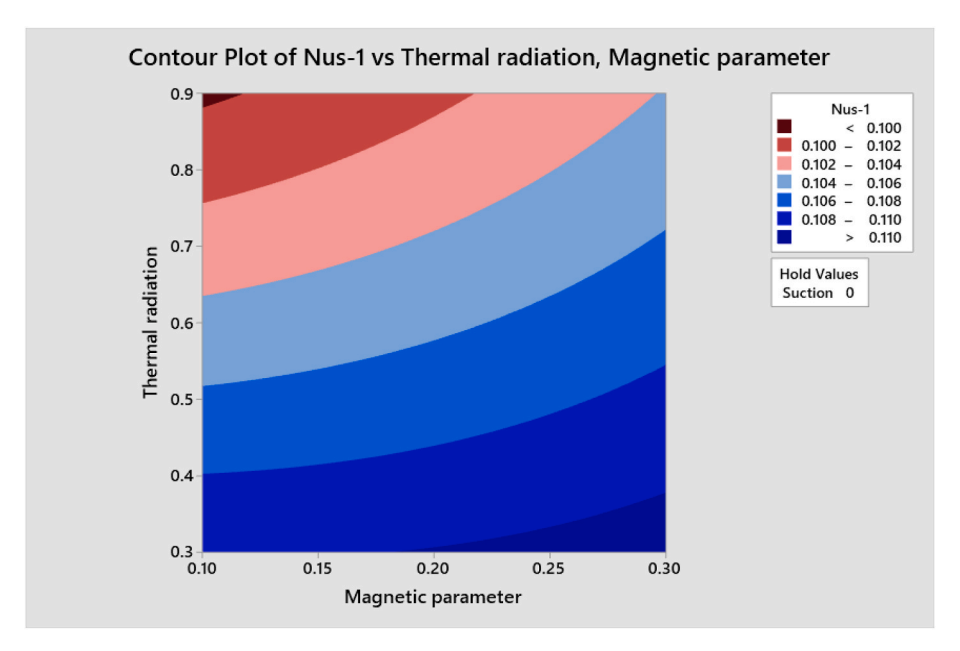


**Fig:15.** Contour Map of Nus - 1 with the influence of N and M.

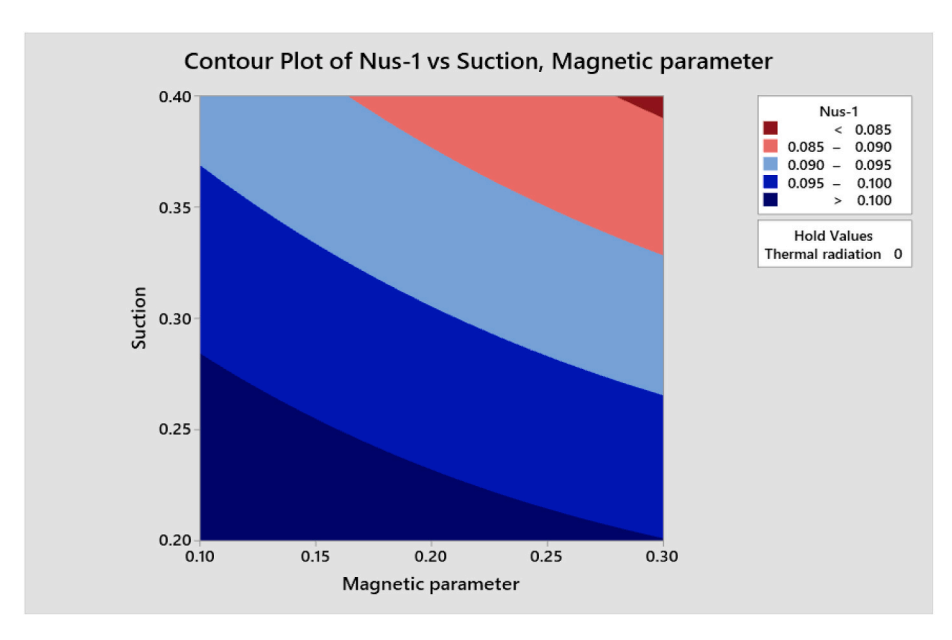


**Fig:16.** Contour Map of Nus - 1 with the influence of S and M.

For thermal radiation, use the Roseland approximation.  $q_r''=-\frac{4\sigma_1}{3k^*}\frac{\partial T^4}{\partial y}$ ,  $\sigma_1$  Constant of Stefan-Boltzmann,  $k^*$  Average absorption ratio. The thermophysical characteristics are as follows:

The ternary hybrid nanoparticles, shaped like spheres, cylinders, and platelets, exhibit viscosities and heat conductivities that are

$$\mu_{hnf} = \left(\mu_{nf3}\phi_3 + \mu_{nf2}\phi_2 + \mu_{nf1}\phi_1\right)\varphi^{-1} \tag{4}$$

$$k_{hnf} = (k_{nf3}\varphi_3 + k_{nf2}\varphi_2 + k_{nf1}\varphi_1)\varphi^{-1}$$
(5)

The density  $(\rho_{\mathit{hnf}})$  of Ternary hybrid nanofluid, which contains nanoparticles in the shapes of spheres, platelets, and cylindrical, is provided by

$$\rho_{hnf} = (1 - \phi_3 - \phi_2 - \phi_1)\rho_{bf} + \phi_3\rho_{sp3} + \phi_2\rho_{sp2} + \phi_1\rho_{sp1}$$
(6)

$$\begin{split} &(\rho\beta_0)_{hnf} = (1 - \varphi_3 - \varphi_2 - \varphi_1)(\rho\beta_0)_{bf} + \varphi_3(\rho\beta_0)_{sp3} + \varphi_2(\rho\beta_0)_{sp2} \\ &+ \varphi_1(\rho\beta_0)_{sp1} \end{split} \tag{7}$$

$$\begin{split} (\rho\beta_1)_{hnf} &= (1 - \phi_3 - \phi_2 - \phi_1)(\rho\beta_1)_{bf} + \phi_3(\rho\beta_1)_{sp3} + \phi_2(\rho\beta_1)_{sp2} \\ &+ \phi_1(\rho\beta_1)_{sp1} \end{split} \tag{8}$$

The Specific heat capacity  $(\rho c_p)_{hnf}$  the source of ternary hybrid nanofluid containing nanoparticles in the shapes of spheres, platelets, and cylindrical is

$$(\rho c_p)_{hnf} = (\rho c_p)_{bf} (1 - \phi_3 - \phi_2 - \phi_1) + \phi_3 (\rho c_p)_{sp3} + \phi_2 (\rho c_p)_{sp2} + \phi_1 (\rho c_p)_{sn1}$$
(9)

The spherical nanoparticles' viscosity and thermal conductivity are:

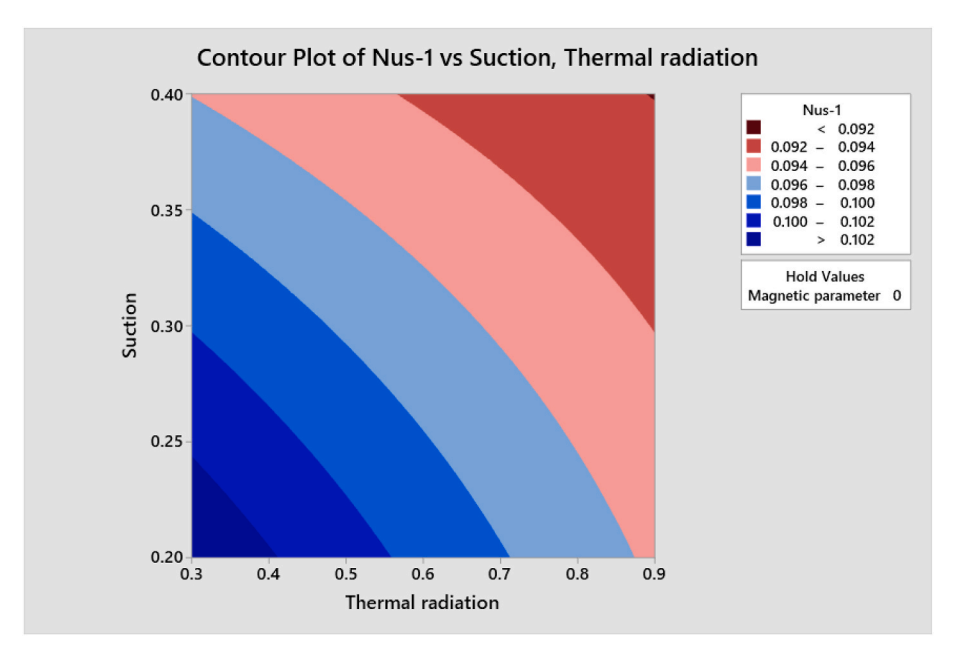
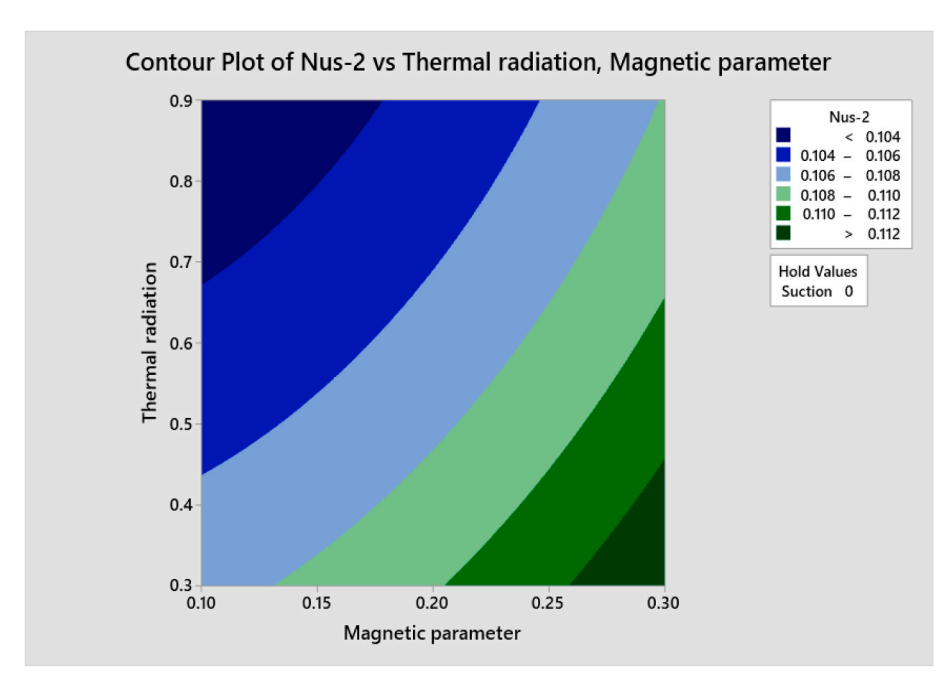


Fig:17. Contour Map of Nus - 1 with the influence of S and N



**Fig:18.** Contour Map of Nus - 2 with the influence of N and M.

$$\mu_{nf1} = (6.2\phi^2 + 2.5\phi + 1) \left(\mu_{bf}\right)$$
(10)

$$\frac{k_{\eta f1}}{k_{bf}} = \left[ \frac{2k_{bf} + k_{sp1} - (k_{bf} - k_{sp1})2\phi}{2k_{bf} + k_{sp1} + (k_{bf} - k_{sp1})\phi} \right]$$
(11)

The cylindrical nanoparticles' viscosity and thermal conductivity are as follows:

$$\mu_{nf2} = (904.4\phi^2 + 13.5\phi + 1)(\mu_{bf})$$
 (12)

$$\frac{k_{nf2}}{k_{bf}} = \left[ \frac{3.9k_{bf} + k_{sp2} - (k_{bf} - k_{sp2})3.9\phi}{3.9k_{bf} + k_{sp2} + (k_{bf} - k_{sp2})\phi} \right]$$
(13)

The thermal viscosity and conductivity of platelet nanoparticles are:

$$\mu_{\eta f3} = \left(612.6\phi^2 + 37.1\phi + 1\right)\left(\mu_{bf}\right) \tag{14}$$

$$\frac{k_{nf3}}{k_{bf}} = \left[ \frac{4.7k_{bf} + k_{sp3} - (k_{bf} - k_{sp3})4.7\phi}{4.7k_{bf} + k_{sp3} + (k_{bf} - k_{sp3})\phi} \right]$$
(15)

The following are the related boundary conditions:

$$v_2 = -v_0, u_2 = 0, T = T_w + c_1 x^{n_1}$$
 at  $y = 0$ 

$$u_2 \to U_2 = (\nu_f x^m) (\delta^{-m-1}), T \to T_\infty \text{ as } y \to \infty$$
 (16)

 $c_1$  and  $n_1$  (Power Index) have constant numbers, and  $\nu_0$  for the suction  $(\nu_0>0)$  and for injection  $(\nu_0<0)$  the rate of fluid flow at the wedge. The expression for potential flow velocity is  $U_2(x,t)=\frac{\nu_f x^m}{8^{m+1}}, \beta_1=\frac{2m}{1+m}$  (see

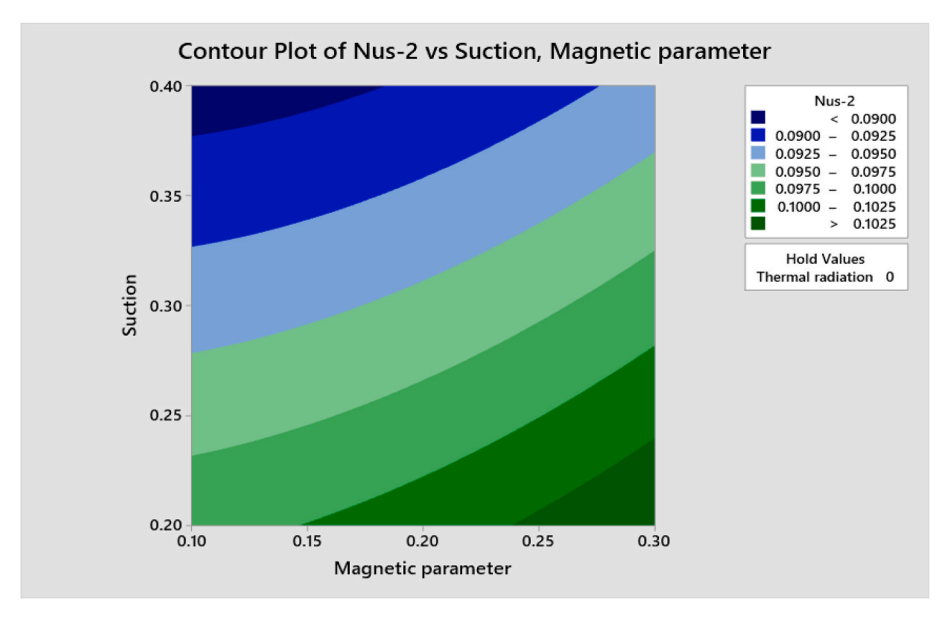


**Fig:19.** Contour Map of Nus - 2 with the influence of S and M.

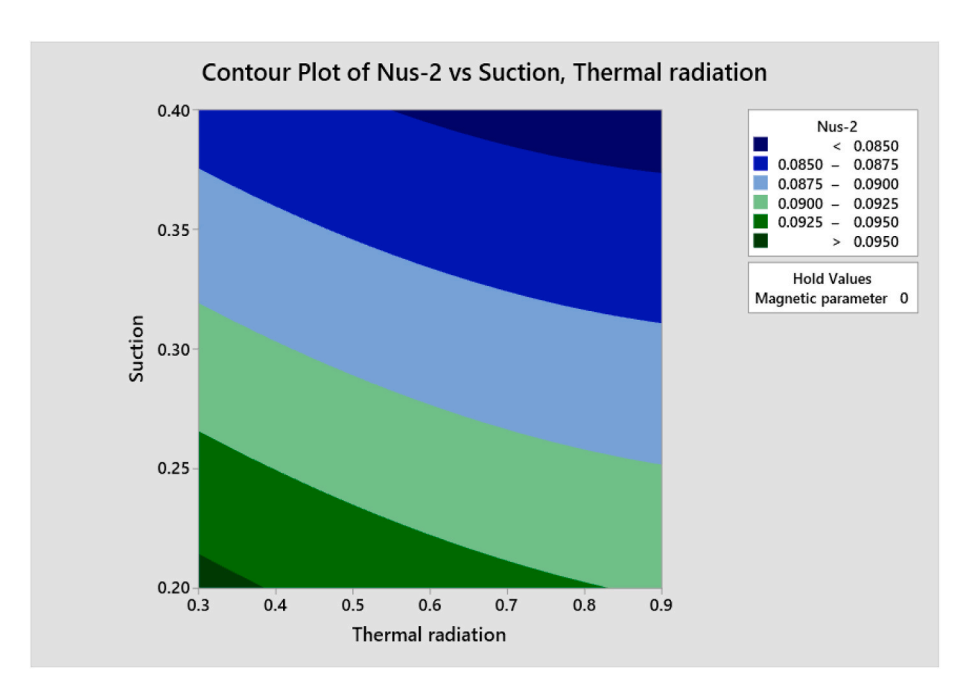


**Fig:20.** Contour Map of Nus - 2 with the influence of S and N.

in Sattar [24])  $\delta$  temporally variable length scale, which is believed to be  $\delta=\delta(t)$  and  $\beta_1$  Hartree pressure gradient parameter, in general  $\beta_1=\frac{\Omega}{\Pi}$  for the overall angle  $\Omega$  Inside the wedge. By Kifissia and Nanoose [25], Stream function is defined as

$$\zeta = \sqrt{\frac{(1+m)}{2}} \sqrt{\frac{x^{m-1}}{\delta^{m+1}}}, \psi = f(\zeta) \frac{\nu_f x^{\frac{m+1}{2}}}{\frac{m+1}{\delta}} \sqrt{\frac{2}{1+m}}, \tag{17}$$

$$\theta = \frac{T - T_{\infty}}{T_{w} - T_{\infty}}, u_{2} = \frac{\partial \psi}{\partial y}, v_{2} = -\frac{\partial \psi}{\partial x}$$
(18)

Equations (2) and (3) are transformed into

$$\begin{pmatrix}
\frac{\partial^{2} \Psi}{\partial t \partial y} + \\
\frac{\partial \Psi}{\partial y} \frac{\partial^{2} \Psi}{\partial x \partial y} - \frac{\partial^{2} \Psi}{\partial y^{2}} \frac{\partial \Psi}{\partial x}
\end{pmatrix} = \frac{1}{G_{2}} \left[ \left\{ G_{5} g \Delta T \sin \frac{\Omega}{2} \theta \right\} + \frac{\nu_{lmf}}{G_{2}} \frac{\partial^{3} \Psi}{\partial y^{3}} + U_{2} \frac{dU_{2}}{dx} - \left( G_{1} \frac{\sigma B_{0}^{2}}{\rho_{nf}} + \frac{\nu_{lmf}}{K} \right) (u_{2} - U_{2}) \right]$$
(19)

$$\left(\frac{\partial \psi}{\partial y}\frac{\partial T}{\partial x} - \frac{\partial \psi}{\partial x}\frac{\partial T}{\partial y} + \frac{\partial T}{\partial t}\right) = \frac{1}{G_4} \left[\frac{1}{\Pr}\left\{G_3\frac{\partial^2 T}{\partial y^2} + \frac{4}{3}N\left((C_T + T)^3\theta'\right)'\right\} - \frac{Q_o\Delta T}{\left(\rho C_p\right)_f}\theta\right]$$
(20)

The following boundary conditions were obtained from Eq. (16).

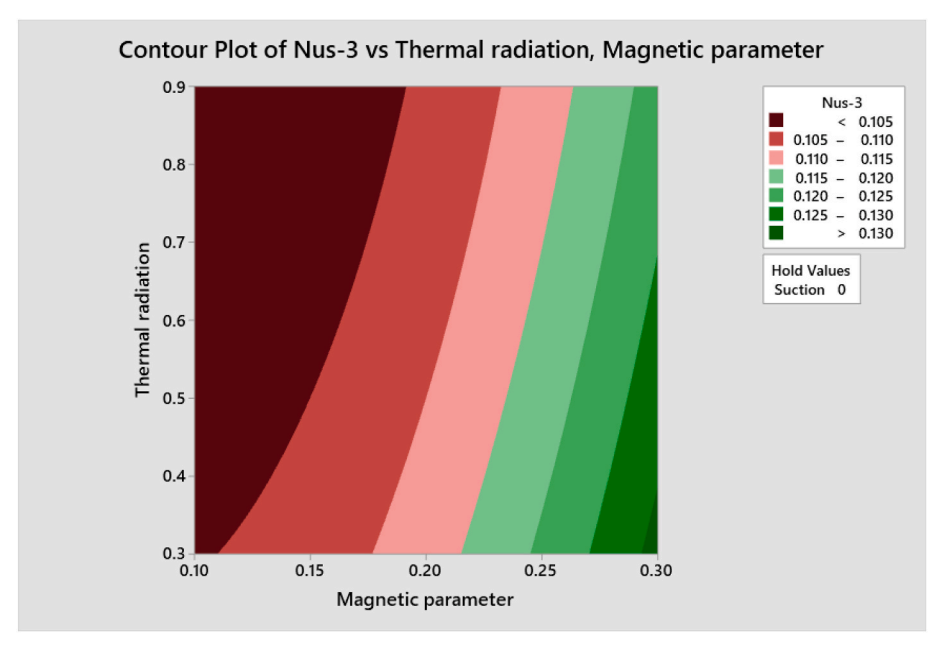


**Fig:21.** Contour Map of Nus - 3 with the influence of N and M.

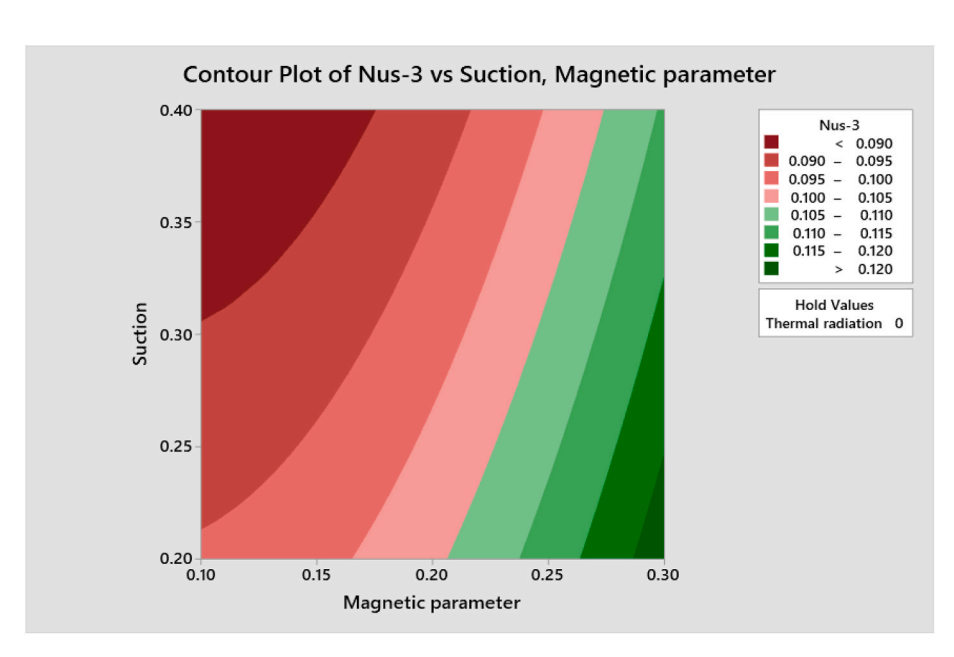


**Fig:22.** Contour Map of Nus - 3 with the influence of S and M.

$$\frac{\partial \psi}{\partial x} = -v_0, \frac{\partial \psi}{\partial y} = 0, T = T_w \text{ at } y = 0 \tag{21}$$

$$\frac{\partial \psi}{\partial y} \rightarrow \frac{\nu x^m}{\delta^{m+1}}, T \rightarrow T_{\infty} \text{ as } y \rightarrow \infty$$
 (22)

 $c_T = \frac{T_\infty}{T_w} - T_\infty$  where the ratio of temperature  $C_T$  By definition, it is predicated on a tiny constant.  $T_w - T_\infty \gg T_\infty$ .

According to this study, it has a valu  $C_T = 0.1$ , Murthy et al. [26]. From a classical Lie group perspective, the symmetry groups of Eqs. (19) and (20) are determined and are defined as

$$\begin{split} \theta^* &= \epsilon \mu_2(x,y,\psi,\theta) + \theta, \\ \psi^* &= \epsilon \mu_1(x,y,\psi,\theta) + \psi, \\ y^* &= y + \epsilon \xi_2(x,y,\psi,\theta), \\ x^* &= x + \epsilon \xi_1(x,y,\psi,\theta) \end{split}$$

Through algebraic methods, infinitesimal formation is

$$\xi_1 = c_2 + c_1 x, \xi_2 = g(x), \mu_1 = c_4 + c_3 \psi \text{ and } \mu_2 = c_5 \theta$$

g(x)-The definitions of the arbitrary functions and infinitesimal generators are  $X_3 = g(x) \frac{\partial}{\partial y} + \frac{\partial}{\partial \psi}, X_2 = \frac{\partial}{\partial x} + g(x) \frac{\partial}{\partial y}, X_1 = \theta \frac{\partial}{\partial \theta} + \psi \frac{\partial}{\partial \psi} + x \frac{\partial}{\partial x} + g(x) \frac{\partial}{\partial y}$ .

Lie group transformation is an example of Lie group symmetry group transformation, with infinitesimal one-parameter to transform the supplied PDEs into a system of ODES.

The formulas for defining characteristics are

$$\frac{d\theta}{\theta} = \frac{dy}{0} = \frac{dx}{x} = \frac{d\psi}{\psi} \tag{23}$$

By solving the equations, we arrive at

$$\psi = xf(\zeta), \zeta = y, \theta = x\theta(\zeta), where \zeta = \zeta(x,t)$$
 (24)

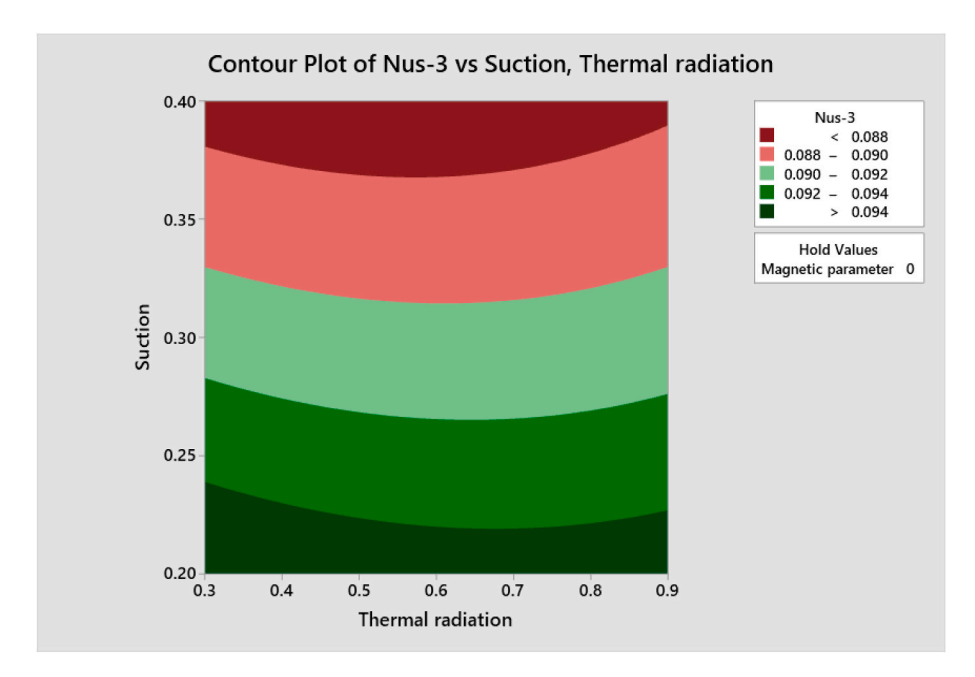


**Fig:23.** Contour Map of Nus - 3 with the influence of S and N.

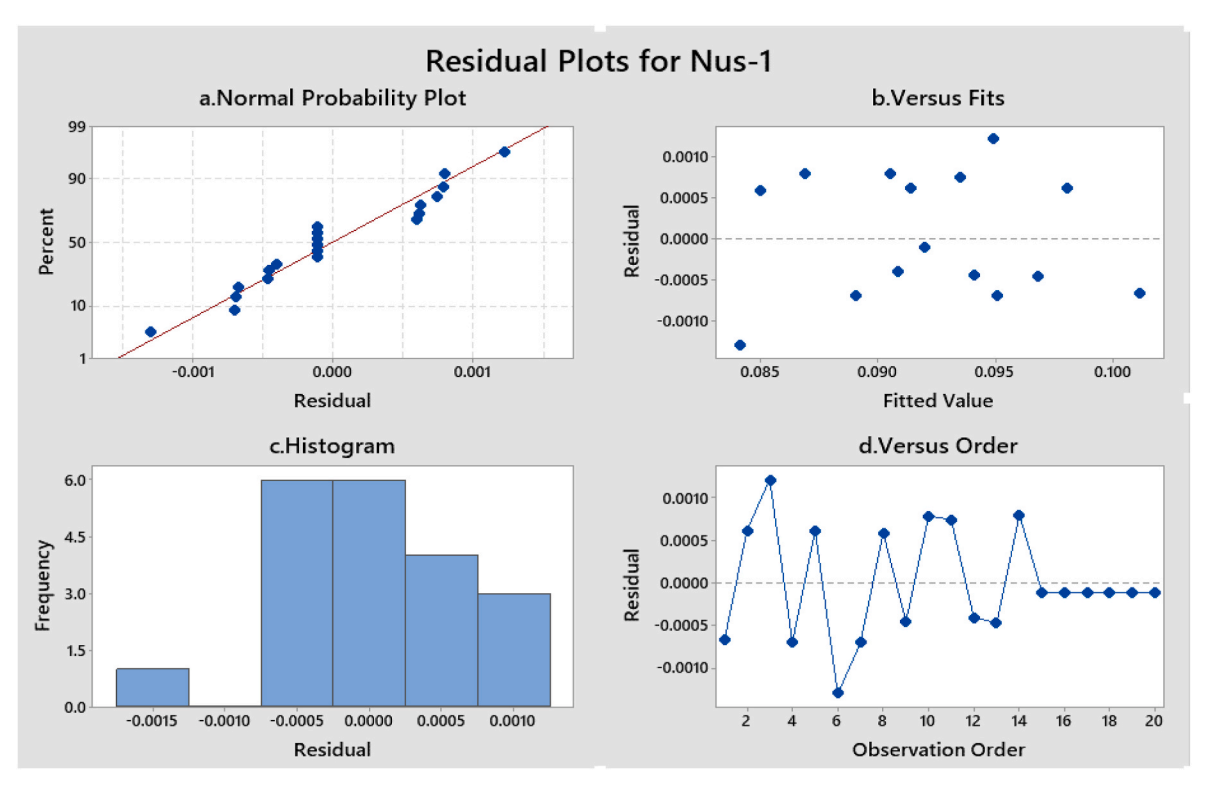


Fig:24. (a) Normal probability plot (b) Versus Fits (response in Nus - 1) (c) Histogram (response in Nus - 1) (d) Versus order (response in Nus - 1).

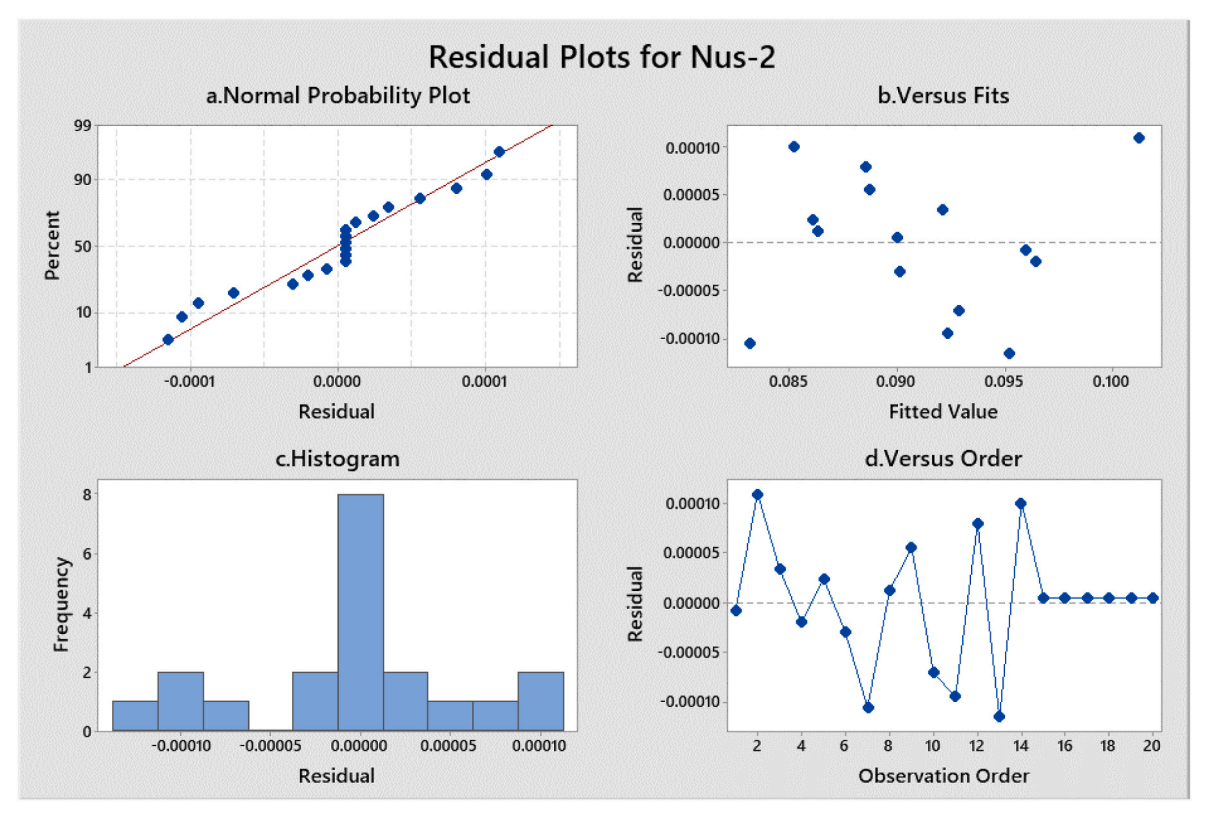


Fig:25. (a) Normal probability plot (b) Versus Fits (response in Nus - 2) (c) Histogram (response in Nus - 2) (d) Versus order (response in Nus - 2).

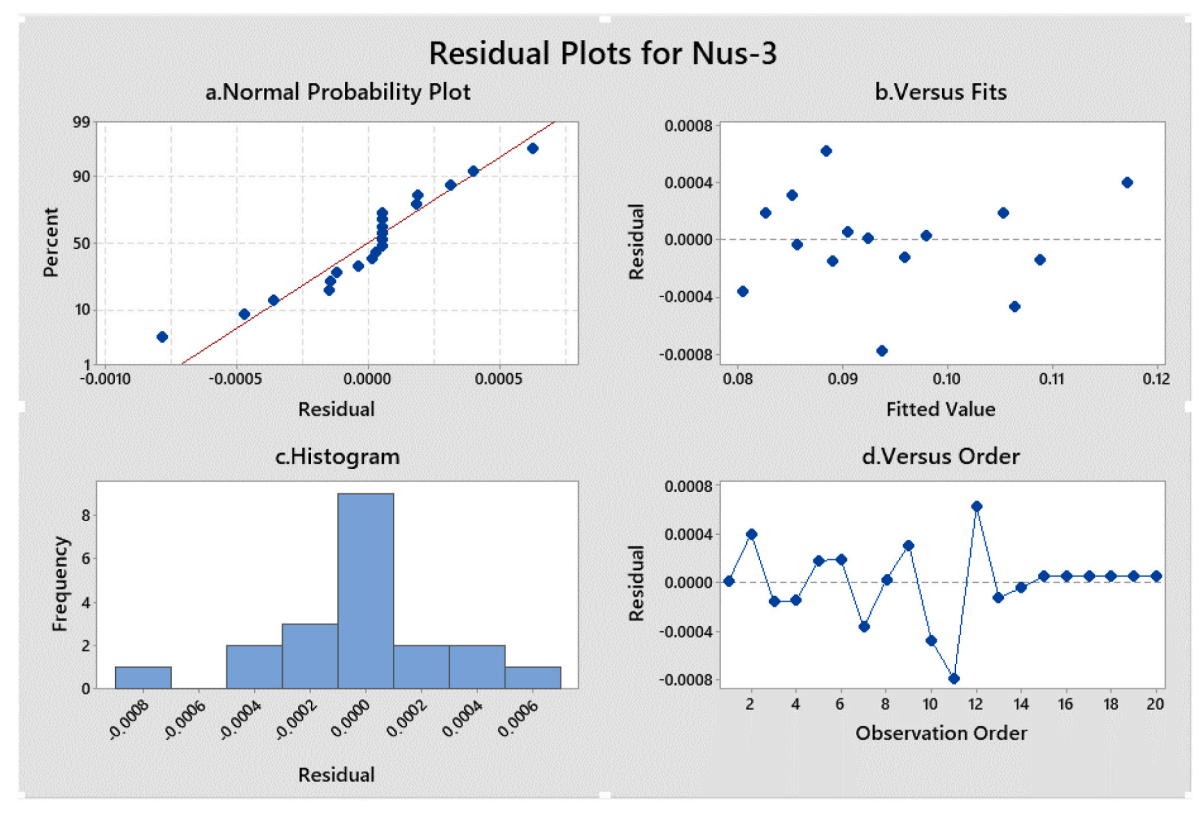
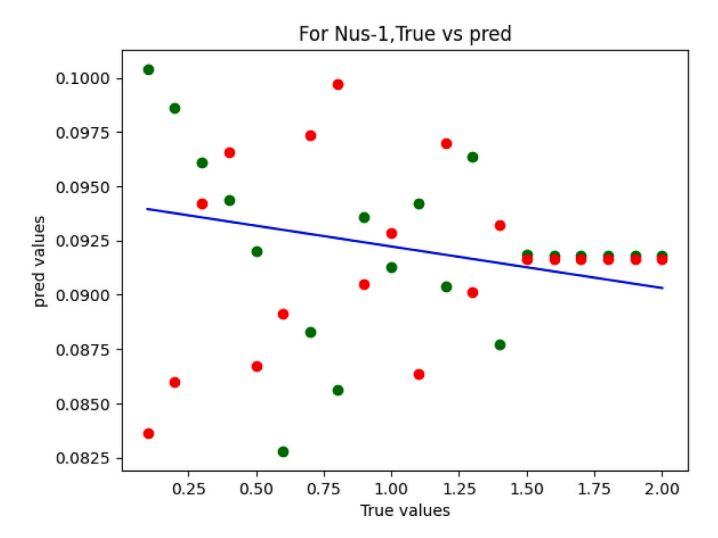
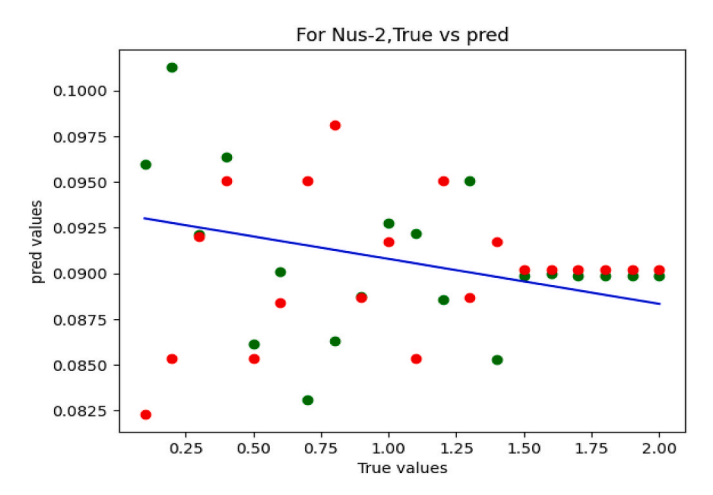


Fig:26. (a) Normal probability plot (b) Versus Fits (response in Nus – 3) (c) Histogram (response in Nus – 3) (d) Versus order (response in Nus – 3).



**Fig:27.** Comparison between expected and observed values for Nus - 1.



 $\textbf{Fig:28.} \ \ \text{Comparison between expected and observed values for \textit{Nus}-2.}$ 

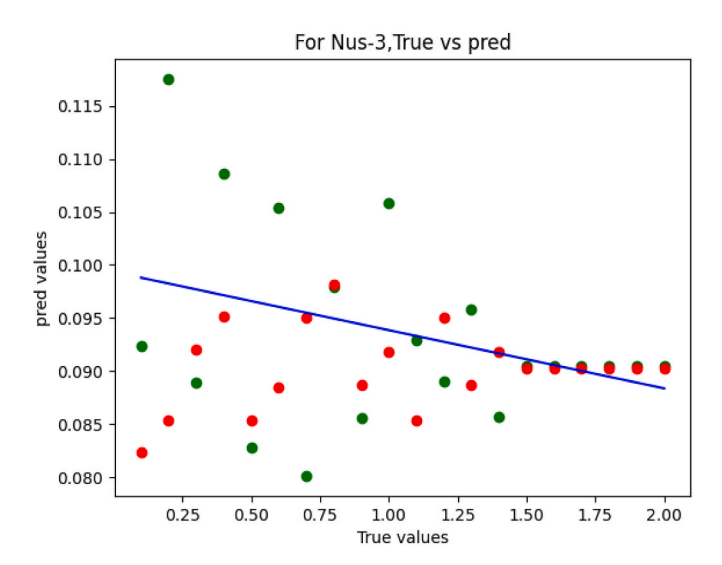


Fig:29. Comparison between expected and observed values for Nus-3.

Here is the outcome of equations (19) and (20)

$$\begin{split} f''' + G_1 G_2 \xi^2 \left[ f f'' + ( \\ & - 2 + 2 f' + \zeta f'') \lambda_v + \left( 1 - f^2 \right) \frac{2m}{m+1} \right] + \frac{2}{m+1} \left[ \left\{ (G_1 G_5) \right\} \times \xi^{\frac{1}{1-m}\gamma} \sin \frac{\Omega}{2} \theta \right. \\ & - \left( (MG_1 + \lambda)(f' - 1) \right] + (G_2 G_1) \frac{1-m}{1+m} \xi \frac{\partial f}{\partial \xi} \left( \frac{\partial f}{\partial \zeta} - \frac{\partial^2 f}{\partial \zeta^2} \right) = 0 \end{split} \tag{25}$$

$$\theta'' + \frac{4}{3G_3} N \left\{ (c_T + \theta)^3 \theta' \right\}'$$

$$- \left( \frac{\Pr G_4}{G_3} \right) \begin{bmatrix} \frac{2n_1}{m+1} f \theta + \frac{2}{1+m} \delta_1 \theta + \lambda_v \zeta \theta' - f \theta' + \\ -\xi \frac{\partial \theta}{\partial \zeta} \frac{\partial f}{\partial \xi} + \xi \frac{\partial f}{\partial \zeta} \frac{\partial \theta}{\partial \xi} \right\} \frac{1-m}{1+m}$$

$$(26)$$

The following conditions apply at the boundaries:

$$\frac{\partial f}{\partial \zeta} = 0, \frac{m+1}{2}f + \frac{1-m}{2}\xi \frac{\partial f}{\partial \xi} = -S, \theta = 1 \text{ at } \zeta = 0$$
 (27)

$$\frac{\partial f}{\partial \zeta} = 1, \theta \to 0 \text{ as } \zeta \to \infty$$
 (28)

Pr =  $\frac{v_f}{a_f}$  is the Prandtl number,  $\lambda = \frac{\delta^{m+1}}{Kk^2}$  Porous media parameter,  $N = \frac{4\sigma_1\theta_s^3}{k_h\eta_p k^e}$  parameter for thermal radiation,  $\theta_w = \frac{1}{T_w - T_\infty}$ .  $\gamma = \frac{g(\rho\beta)\Delta T}{\rho_f U^2 k^{1-m}}$  Is buoyancy or the natural convention parameter,  $\delta_1 = \frac{Q_0v_f^2}{k_f U_2^2}\Delta T$  is the heat source/sink parameter, and  $M = \frac{\sigma B_0^2}{H_f} \frac{\delta^{m+1}}{k^2}$  the magnetic parameter,  $S = -V_0\sqrt{\frac{(1+m)x}{2\nu U_2}}$  is injection if S < 0 and Suction parameter if S > 0 and  $\xi = \frac{x^2-m}{2}$ , According to Kifissia and Nanoose [25], the wedge with no dimensions located along  $(\xi > 0)$ . The terms in this system of equations with partial derivatives describe the non-similarity qualities of the situation  $\xi$ , this problem prohibits solutions based on similarities. Thus, with  $\xi$ -The terms that are accompanied in the first level are abbreviated by  $\frac{\partial}{\partial \xi}$  are tiny. This is definitely the case when  $(\xi \ll 1)$ . Thus, the term with  $\xi$   $\frac{\partial}{\partial \xi}$  the system of equations that results after the right-hand side of Equations (25) and (26) is removed is as follows.

$$\begin{split} f''' + & (G_1 G_2) \left[ f f'' + \lambda_v ( \\ & - 2 + \zeta f'' + 2f') + \left( 1 - f^2 \right) \frac{2m}{m+1} \right] + \frac{2}{m+1} \left[ \left\{ (G_5 G_1) \right\} \times \gamma \sin \frac{\Omega}{2} \theta \right. \\ & - & \left. (MG_1 + \lambda)(f' - 1) \right] = 0 \end{split} \tag{29}$$

$$\theta'' + \frac{4}{3G_3}N\left\{(c_T + \theta)^3\theta'\right\}' - \left(\frac{\Pr G_4}{G_3}\right)\left[\frac{2n_1}{m+1}f'\theta\right]$$
$$-f\theta' + \lambda_v\zeta\theta' + \frac{2}{1+m}\delta_1\theta = 0$$
(30)

The following are the boundary circumstances:

$$\theta = 1, f = 0, f = -\frac{2S}{m+1}$$
 at  $\zeta = 0$  (31)

$$f = 1, \theta \to 0 \text{ as } \zeta \to \infty$$
 (32)

Let  $\lambda_v = \frac{c}{\chi^{m-1}}$ , where  $c = \frac{\delta^m}{v_f} \frac{\partial \delta}{\partial t}$  are integrating,  $\delta = \left[v_f t c(m+1)\right]^{\frac{1}{m+1}}$ . When m=1 and c=2 in  $\beta_1$ , we get  $\delta = 2\sqrt{v_{\phi}t}$  which obtains the parameter and which is given the parameter  $\delta$ . It is analogous to the scaling parameter that is known for unstable boundary layer problems (see Schlichting [27]).

**Table 2**The physical parameter values for the skin friction coefficient.

											Skin friction		
$\varphi$	S	M	N	λ	$\lambda_{\gamma}$	$\delta_1$	$\overline{n_1}$	m	$\overline{C_T}$	γ	Case-1	Case-2	Case-3
0.001											0.003070	0.006378	0.010434
0.002											0.004030	0.007260	0.011307
0.003											0.005355	0.008233	0.012231
	0.2										0.009880	0.004228	0.004864
	0.3										0.009699	0.005574	0.006040
	0.4										0.010963	0.006771	0.007133
		0.1									0.002957	0.000311	0.003328
		0.2									0.006425	0.002855	0.001463
		0.3									0.010963	0.006771	0.007133
			0.3								0.002442	0.000095	0.002352
			0.6								0.002441	0.000094	0.002353
			0.9								0.002441	0.000093	0.002355
				0.1							0.010963	0.006771	0.007133
				0.3							0.012885	0.019338	0.021786
				0.5							0.009017	0.005394	0.054631
					0.4						0.001517	0.017425	0.095664
					0.5						0.004789	0.007192	0.454268
					0.6						0.003225	0.099426	0.040936
						0.3					0.010963	0.006771	0.007133
						0.4					0.003642	0.006776	0.007139
						0.5					0.006849	0.006779	0.007144
							0				0.004080	0.006771	0.007132
							0.02				0.006850	0.006771	0.007132
							0.04				0.002982	0.006771	0.007133
								1.5			0.004414	0.010692	0.010227
								2			0.004112	0.011395	0.014447
								2.5			0.003870	0.011762	0.016276
									0.2		0.001980	0.019611	0.021542
									0.5		0.003056	0.021645	0.021540
									0.7		0.005073	0.021427	0.021539
										0.5	0.010963	0.006771	0.007133
										1	0.006704	0.006712	0.007044
										1.5	0.006779	0.006653	0.006955

The Nusselt number and the skin friction coefficient are described as

$$c_f = \left(\frac{\partial u_2}{\partial y}\right)_{y=0} \frac{\mu_{Thinf}}{\rho_f U_2^2} = -G_2(Re_x)^{-\frac{1}{2}} f''(0)$$

$$Nu_x = \frac{xk_{Thnf}}{k_f(T_w - T_\infty)} \left(\frac{\partial T}{\partial y}\right)_{y=0}$$

$$= -G_4(\text{Rex})^{\frac{1}{2}}\theta'(0)\left[1 + \frac{4}{3}N(c_T + \theta(0))^3\right]$$

The local number for Reynolds is  $Re_x = \frac{U_x}{v_f}$ .

Similar transformations are employed in Equations (29) and (30).

$$G_{1} = \frac{\rho_{hnf}}{\rho_{f}}, G_{2} = \frac{\mu_{hnf}}{\mu_{f}}, G_{3} = \frac{\left(\rho c_{p}\right)_{hnf}}{\left(\rho c_{p}\right)_{f}}, G_{4} = \frac{k_{hnf}}{k_{bf}}, G_{5} = \frac{\left(\rho \beta\right)_{hnf}}{\rho_{f}}$$

# 3. Numerical approach

The results are obtained with different parameter ranges using the BVP5C approach; adjustment is made for the step size of  $\eta$  is  $\Delta\eta$ , and the edge of the boundary layer,  $\eta_{\infty}$ . Here, step size  $\Delta\eta=0.01$  with tolerance  $10^{-6}$ .

Higher-order governing equations (29) and (30) are converted to lower-order equations by choosing the suitable assumptions as follows:

$$f = h_1, f' = h_2, f'' = h_3, \theta = h_4, \theta' = h_5$$

**Boundary Conditions:** 

$$f_a(2) = 1, f_a(1) = 0, f_4(4) = 1$$
  
 $f_b(2) = 0, f_b(4) = 0$ 

# 4. Results analysis and discussion

The heat transfer through a moving porous wedge in the presence of thermal radiation, a Darcy ternary hybrid nanofluid flow, a magnetic field, and heat radiation is reported in this paper. To investigate the effects of various physical characteristics on temperature and velocity distributions, contour plots for Nusselt numbers-1, 2, and 3 are shown in Figs. (2) to (29). Wherein Tables 1–5 lists the thermophysical parameters of the base fluid and nanoparticles. Cases: 1 AA7072: Polyethylene Glycol-Water: 2 AA7072+ Zirconium oxide: Polyethylene Glycol-Water: and 3 AA7072+ Zirconium oxide + Magnesium oxide: Polyethylene Glycol-Water. The physical parameter values for the skin friction coefficient are shown in Table 2. The physical parameter values for the local Nusselt number are displayed in Tabe:3. Key RSM parameters are included in Table 4, along with their levels and symbols. An illustration of a comparison of numerical results by applying RSM and machine learning results drawn by Gradient descent technique and Table 6a,b The variance analysis was investigated for Nus.

The velocity and temperature distributions for various nanofluid, hybrid, and ternary hybrid nanofluid situations are impacted by the nanoparticle volume fraction parameter shown in Figs. 2 and 3. An increase in nanoparticle volume fraction causes the fluid's temperature to drop and its velocity to rise. This occurs because increased nanoparticle volume fraction results in a higher fluid density and enhanced convective heat transfer, which lowers fluid temperature because of higher heat dissipation. The behaviour of the thermal field when the other parameter values stay constant at = 0.2, 0.3, and 0.4 is shown in Fig. 4. When it comes to ternary hybrid, hybrid, and nanofluid, the temperature drops due to a rising trend S. The thermal boundary layer thickens when the fluid temperature decreases to the free stream temperature from the wall. Boundary heat transfer coefficient is affected by increases in the suction/injection parameter. The heat transfer coefficient measures the

Results in Engineering 23 (2024) 102714

**Table 3**The physical parameter values for the local Nusselt number.

$\varphi$											Nusselt numb	er	
	S	M	N	λ	$\lambda_{\gamma}$	$\delta_1$	$\overline{n_1}$	m	$\overline{C_T}$	γ	Case-1	Case-2	Case-3
0.001											0.001983	0.003963	0.005994
0.002											0.001927	0.003914	0.005947
0.003											0.001848	0.003860	0.005897
	0.2										0.002583	0.006541	0.010012
	0.3										0.002148	0.005432	0.008403
	0.4										0.001692	0.004533	0.007076
		0.1									0.002282	0.004939	0.007630
		0.2									0.002035	0.004759	0.007378
		0.3									0.001692	0.004533	0.007076
			0.3								0.002863	0.005951	0.009128
			0.6								0.002554	0.005294	0.008116
			0.9								0.002365	0.004894	0.007498
				0.1							0.001692	0.004533	0.007076
				0.3							0.001457	0.003826	0.006299
				0.5							0.001904	0.003934	0.004775
					0.4						0.002000	0.002900	0.003206
					0.5						0.001751	0.003227	0.005301
					0.6						0.001683	0.000449	0.003964
						0.3					0.001692	0.004533	0.007076
						0.4					0.003329	0.006726	0.010368
						0.5					0.004130	0.008657	0.013272
							0				0.002180	0.004537	0.007059
							0.02				0.001995	0.004536	0.007063
							0.04				0.002239	0.004535	0.007066
								1.5			0.000965	0.001958	0.003444
								2			0.000838	0.001676	0.002766
								2.5			0.000742	0.001470	0.002377
									0.2		0.002008	0.003023	0.005242
									0.5		0.001900	0.002922	0.005110
									0.7		0.001722	0.002929	0.005072
										0.5	0.001692	0.004533	0.007076
										1	0.001995	0.004536	0.007081
										1.5	0.001989	0.004539	0.007085

**Table 4**Important RSM parameters, together with their symbols and levels.

Key factors	Symbols	Levels		
		-1 (Low)	0 (Medium)	1 (High)
M	$X_1$	0.1	0.2	0.3
N	$X_2$	0.3	0.6	0.9
S	$X_3$	0.2	0.3	0.4

rate energy moves from the wall to the fluid, or vice versa. More fluid is injected into the wall as the suction/injection parameter rises. This suggests that the fluid near the wall can reach the wall temperature faster than in the absence of suction or injection. Because of this, in contrast to the other two fluid scenarios, the thermal boundary layer thins in the ternary hybrid nanofluid case.

In the cases of nanofluid, hybrid, and ternary nanofluid, the fluid temperature is lowered by the magnetic field parameter by boosting convection, accelerating convective heat transfer, and increasing heat dissipation. This helps to balance any localized magnetic heating effects (see Fig. 5). Thermal radiation decreases the temperature distribution, as depicted in Fig. 6. Heat radiation and thermal conduction have an inverse correlation. As a result, the ternary hybrid nanofluid transfers less heat since thermal radiation releases most of the heat from the system, which can increase the pressure in a wedge. It is essential to ensure that a positive number shows an internal heat source, whereas negative values show a heat sink. We have selected the values of  $\delta_1$  as 0.3, 0.4, and 0.5 in the following manner. By examining Fig. 7, it becomes evident that raising the values of  $\delta_1 > 0$  leads to the release of energy and increasing temperature. and aconverselyincreasingthevalues of  $\delta_1 < 0$  causes energy absorption, leading to a drop in temperature distribution in nanofluid in contrast to ternary hybrid nanofluid and

hybrid nanofluid instances. It is also observed that thermal radiation produces a better temperature distribution when it is present than when it is absent. Fig. 8 depicts the relationship between temperature and porosity parameters for ternary hybrid nanofluids. As the level of porosity increases, the temperature lowers progressively. Higher porosity results in enhanced heat dissipation efficiency. In addition, the thermal boundary layer becomes thinner as porosity increases, suggesting a denser thermal boundary with higher porosity.

Fig. 9 proves that the buoyancy coefficient  $\gamma$  effects the temperature distribution. As the buoyancy parameter increases, the thermal boundary-layer thickness drops because of a higher heat transfer rate, usually the buoyant force to viscous force ratio. When the temperature drops, the buoyancy increases the temperature gradient and rate of heat transfer. Fig. 10 illustrates that the temperature of the three fluids decreases when the hall current parameter is used. m values of 1.5, 2, and 2.5 increase. The temperature decrease is convincing for  $0 \le \zeta \le 5$ . Hybrid nanofluids have a higher temperature than ordinary nanofluids. The ternary hybrid nanofluid exhibits higher thermal conductivity than nanofluid and hybrid nanofluids, increasing temperature. Fig. 11 shows the temperature ratio parameter.  $C_T$  on temperature distribution. The temperature ratio parameter escalates the temperature of the fluid in all three cases. This figure demonstrates that in nanofluid situations, as opposed to hybrid and ternary nanofluid cases, Significant improvement is shown in the thickness of the thermal boundary layer. The impact is demonstrated in Fig. 12, where it is evident that for all three scenarios analysed, there is a significant decrease in both the temperature of the fluid and the thickness of the thermal boundary layer. This suggests that, despite the variations in conditions among these cases, there is a constant pattern of temperature decrease and reduction in the thickness of the thermal boundary layer. This behaviour indicates enhanced thermal efficiency and more efficient heat dissipation inside the fluid. The power law index impacts the dimensionless temperature and velocity in

Results in Engineering 23 (2024) 102714

Table 5

Comparison of numerical results by applying RSM and machine learning results drawn by Gradient descent technique.

Runs	ns Coded values			Real v	alues		Response						
	$X_1$	$X_2$	$X_3$	M	N	S	Nus-1		Nus-2		Nus-3		
							True values	Predicted values	True values	Predicted values	True values	Predicted values	
1	-1	-1	-1	0.1	0.3	0.2	0.1004	0.083618	0.09595	0.0823051	0.092333	0.084631	
2	1	-1	-1	0.3	0.3	0.2	0.0986	0.085991	0.10129	0.0853674	0.117548	0.089371	
3	-1	1	-1	0.1	0.9	0.2	0.0961	0.094219	0.09212	0.0920223	0.088894	0.093726	
4	1	1	-1	0.3	0.9	0.2	0.09438	0.096592	0.09639	0.095084	0.108602	0.09846	
5	-1	-1	1	0.1	0.3	0.4	0.0920	0.08674	0.08612	0.0853550	0.082811	0.087750	
6	1	-1	1	0.3	0.3	0.4	0.0828	0.089112	0.09007	0.0884173	0.105418	0.092490	
7	$^{-1}$	1	1	0.1	0.9	0.4	0.0883	0.097341	0.08308	0.0950722	0.080098	0.096845	
8	1	1	1	0.3	0.9	0.4	0.08560	0.099713	0.08630	0.0981345	0.09797	0.101585	
9	$^{-1}$	0	0	0.1	0.6	0.3	0.09360	0.09048	0.08874	0.0886886	0.085496	0.090738	
10	1	0	0	0.3	0.6	0.3	0.0913	0.092852	0.09277	0.0917510	0.105869	0.095478	
11	0	$^{-1}$	0	0.2	0.3	0.3	0.09424	0.086365	0.0922	0.085361	0.092893	0.08856	
12	0	1	0	0.2	0.9	0.3	0.09041	0.096966	0.08859	0.0950784	0.089022	0.097656	
13	0	0	-1	0.2	0.6	0.2	0.096339	0.090105	0.09506	0.0886948	0.095775	0.091549	
14	0	0	1	0.2	0.6	0.4	0.0877	0.093227	0.08528	0.0917448	0.085608	0.094668	
15	0	0	0	0.2	0.6	0.3	0.09187	0.091666	0.0899	0.090219	0.090494	0.09310	
16	0	0	0	0.2	0.6	0.3	0.0918	0.091666	0.08998	0.0902198	0.090494	0.09310	
17	0	0	0	0.2	0.6	0.3	0.0918	0.091666	0.0899	0.090219	0.090494	0.09310	
18	0	0	0	0.2	0.6	0.3	0.0918	0.091666	0.0899	0.090219	0.090494	0.09310	
19	0	0	0	0.2	0.6	0.3	0.0918	0.091666	0.0899	0.090219	0.090494	0.09310	
20	0	0	0	0.2	0.6	0.3	0.0918	0.091666	0.0899	0.0902198	0.090494	0.09310	

**Table 6(a)**The variance analysis was investigated for Nus.

Source	Degrees of freedom	Adjusted Sun	n of squares	Adjusted Mea	an square	F-value		P-value	
		Case-1	Case-2	Case-1	Case-2	Case-1	Case-2	Case-1	Case-2
Model	9	0.000317	0.000339	0.000035	0.000038	42.72	5107.12	0	0
Linear	3	0.000012	0.000007	0.000004	0.000002	4.7	316.65	0.027	0
M	1	0	0	0	0	0.34	1.66	0.57	0.227
N	1	0.000006	0.000002	0.000006	0.000002	7	285.21	0.025	0
S	1	0.000001	0.000003	0.000001	0.000003	1.37	350.33	0.268	0
Square	3	0.000001	0.000008	0	0.000003	0.27	355.64	0.849	0
M * M	1	0	0.000002	0	0.000002	0.31	229.93	0.59	0
N * N	1	0	0.000001	0	0.000001	0.11	75.15	0.752	0
S*S	1	0	0	0	0	0.06	14.62	0.818	0.003
2-way Interaction	3	0.000022	0.000002	0.000007	0.000001	8.8	72.87	0.004	0
M * N	1	0.000005	0	0.000005	0	6.5	55.6	0.029	0
N * S	1	0.000009	0.000001	0.000009	0.000001	10.78	100.32	0.008	0
S*M	1	0.000008	0	0.000008	0	9.13	62.68	0.013	0
Error	10	0.000008	0	0.000001	0				
Lack of fit	5	0.000008	0	0.000002	0	*	*	*	*
Pure error	5	0	0	0	0				
Total	19	0.000325	0.000339						
$R^2 =$	97.46 %								

Figs. 13 and 14. We observe that a rise in the power law index values results in a velocity across a wedge. It is seen that the temperature distribution gradually rises after falling at first.

Contour plots are two-dimensional graphical representations of three-dimensional data that join points of similar value using contour lines. In disciplines like meteorology, geology, and engineering, they are frequently used to depict the topography of a surface or the levels of a particular variable. Figs. 15, 18 and 21 represent the variations of Nusselt numbers for nanofluid (Nus-1), hybrid nanofluid (Nus-2), and ternary hybrid nanofluid (Nus-3) about variations in the magnetic field and radiation parameters, when the suction parameter is absent. Increasing causes an increase in Nus-1, Nus-2, and Nus-3; its highest value is observed at 0.30, and its lowest value is 0.10 for the smallest amount of 0.3 and the most significant amount of 0.9, respectively. The enhanced heat transfer mechanism in nanofluids is attributed to the heat radiation characteristics and the strengthening effect of the magnetic field. The improved heat transfer results result from the disturbance in fluid flow caused by the magnetic field and the ability of nanoparticles to absorb thermal radiation, which leads to an increase in the Nusselt number. Our analysis determined that the heat transfer rate is more

significant in ternary hybrid nanofluid than in hybrid and nanofluid cases. Figs. 16, 19 and 22 illustrate that the Nus-2, Nus-1and Nus-3 on the suction parameter (0.20-0.40) and magnetic field parameter (0.10-0.30) when the thermal radiation parameter is absent. The trihybrid nanofluid case exhibits an enhanced heat transfer rate, as evidenced by the contour plots, due to improved fluid flow and a reduced thermal boundary layer. The suction parameter and the magnetic field parameter without heat radiation increase the Nusselt number. These properties lead to improved heat transport, which raises the Nusselt number. Figs. 17, 20 and 23 describe the Nus-1, Nus-2, and Nus-3 on thermal radiation and suction parameters (0.10-0.30) without magnetic field parameters. Variations in the suction and heat radiation parameters in trihybrid nanofluids increase the Nusselt number, quantifying convective heat transfer. In particular, increasing the suction value increases fluid flow, while increasing the thermal radiation parameter accelerates heat transmission by convection in the nanofluid. Due to these enhancements, the Nusselt number has increased.

Figs. 24–26 show and allow access to these residual charts. The average probability plots of the residuals show outstanding conditions based on these statistics. Unlike a symmetrical distribution, the residual

**Table:6(b)**The variance was investigated for Nus.

Source	Degrees of freedom	Adjusted Sum of squares	Adjusted Mean square	F-value	P-value
		Case-3	Case-3	Case-3	Case-3
Model	9	0.001642	0.000182	1033.12	0
Linear	3	0.000018	0.000006	34.63	0
M	1	0.000006	0.000006	31.53	0
N	1	0.000001	0.000001	8.18	0.017
S	1	0.000003	0.000003	17.13	0.002
Square	3	0.000175	0.000058	329.72	0
M * M	1	0.000078	0.000078	440.94	0
N * N	1	0.000001	0.000001	5.54	0.04
S*S	1	0	0	1.7	0.221
2-way Interaction	3	0.000016	0.000005	30.57	0
M * N	1	0.000013	0.000013	74.24	0
N * S	1	0.000002	0.000002	13.98	0.004
S*M	1	0.000001	0.000001	3.5	0.091
Error	10	0.000002	0		
Lack of fit	5	0.000002	0	*	*
Pure error	5	0	0		
Total	19	0.001644			
$R^2 =$	97.46 %				

histograms in these three pictures show a skewed distribution. The observed and fitted values correlate strongly, as the residual diagrams show. The nanofluid, hybrid nanofluid, and trihybrid nanofluid demonstrate the most significant residuals near values of 0.0010, 0.0001, and 0.0006, respectively, for the Nusselt numbers-1, 2, and 3. Finally, Gradient descent is an optimisation method that moves repeatedly in the direction of the steepest descent to optimise a function. It is frequently used in machine learning to determine a model's ideal parameters; the Machine Learning graphs (Figs. 27–29) compare actual and predicted values for the Nusselt numbers of nanofluid, hybrid nanofluid, and trihybrid nanofluid. These figures show us that the Gradient descent technique was able to predict the truth values accurately; Truth values are represented in Green colour and Predicted values are in red colour.

## 5. Conclusion

This study examines a wedge's fluid flow properties, temperature distribution, velocity, and heat transfer rate using natural convection combined with nanofluid, hybrid nanofluid, and ternary nanofluid. The numerical investigation conducted in this research holds great significance in the field as it compares the volume fraction of nanofluids, hybrid nanofluids, and ternary nanofluids. A wedge-shaped surface is necessary to induce the boundary layer flow for heat exchanger systems and geothermal applications.

This investigation yields the following noteworthy findings.

# 5.1. Key findings include

- Nanoparticle volume fraction: The velocity profile rises in ternary hybrid nanofluid compared to the nanofluid, but temperature profiles decrease in nanofluid than in ternary hybrid nanofluid.
- Porosity: As the values of the porosity parameter rise, the velocity profile falls.
- Magnetic field parameter: The temperature profile falls as the magnetic parameter rises due to retardation force.
- Therma radiation: An increase in thermal radiation parameter decelerates the temperature profile.
- **Temperature ratio parameter:** The temperature ratio parameter values rise with a reduction in the temperature profile.
- **Nusselt numbers-1, 2, and 3:** ternary hybrid nanofluids (Case-3) have a higher Nusselt number than hybrid and nanofluids (Case-1).

## 6. Future directions of the work

In the following years, researchers will be able to look at various features of the three-dimensional rotational magnetohydrodynamic tetra hybrid nanofluids that flow through different forms, including spherical, cylindrical, and platelet. These studies will include other combinations of tetra hybrid nanofluids, such as AA7072, zirconium oxide, magnesium oxide, and aluminium oxide combined with polyethene and water. This thorough examination could be expanded upon by looking into the impacts of Brownian motion, thermophoresis, activation energy, Cattaneo-Christov, and hall currents. Furthermore, there are prospects to extend the range of this study by investigating distinct fluid kinds, such as non-Newtonian and tetra-hybrid nanofluids, and investigating sophisticated methods for chemical synthesis and deposition, in addition to several other possible paths for improving the research.

# Conflict of interest that might arise

All of the authors claim to have no conflicting interests.

# CRediT authorship contribution statement

S. Suresh Kumar Raju: Writing – review & editing, Writing – original draft, Funding acquisition. P Durgaprasad: Writing – review & editing, Writing – original draft. José Luis Díaz Palencia: Writing – review & editing, Writing – original draft, Supervision, Conceptualization. Abderrahim Wakif: Writing – review & editing, Methodology. C. S.K. Raju: Writing – review & editing, Methodology. Maddina Dinesh kumar: Writing – original draft, Visualization, Methodology. Muneerah Al Nuwairan: Writing – review & editing, Funding acquisition, Formal analysis. Ali J.Chamkha: Writing – review & editing, Formal analysis.

# Declaration of competing interest

All the authors declare no conflict of interest.

## Data availability

Data will be made available on request.

### Nomenclature:

Symbol	Name
$q_r^{''}$	Roseland approximation
$k^*$	Average absorption
$c_1$	Constant number
$n_1$	Power index
$U_2$	Potential flow velocity
Pr	Prandtl number
M	Magnetic parameter
T	Fluid temperature
$T_w$	Fluid wall temperature
**	Ambient fluid temperature
$T_{\infty}$	
$u_2, v_2$	Velocity components along the x and y-axis
$k_{bf}$	Thermal conductivity of the base fluid
$k_{nf1}$	Thermal conductivity of nanofluid for AA702
$k_{nf2}$	Thermal conductivity of nanofluid for Zirconium Oxide
$k_{nf3}$	Thermal conductivity of nanofluid for Magnesium Oxide
Re <sub>x</sub>	Reynolds number
$C_f$	Skin friction coefficients
Nux	Nusselt number
$B_0$	Magnetic strength
m	Hall current parameter
$C_T$	Temperature ratio
-	Temperature ratio
Greek SymbolsF	Cimilanity youighla
η	Similarity variable
Ψ	Stream function
$\theta$	Dimensionless temperature
$\sigma_1$	Stefan-Boltzmann
$ ho_{hnf}$	Density of ternary hybrid
S	Suction/Injection
$\beta_1$	Hartree pressure gradient
Ω	Overall, all angle within a wedge
$\theta_w$	Thermal radiation
$ u_{bf}$	Kinematic viscosity of base fluid
φ	Nanoparticle volume fraction
$(\rho c_p)_{hnf}$	Hybrid nanoparticle's thermal capacity
•	
$\phi_1$	The nanoparticle volume fraction of AA702
$\phi_2$	Nanoparticle volume fraction of Zirconium Oxide
$\phi_3$	Nanoparticle volume fraction of Magnesium Oxide
$\mu_{nf1}$	Dynamic Viscosity of AA702
$\mu_{nf2}$	Dynamic Viscosity of Zirconium Oxide
$\mu_{nf3}$	Dynamic Viscosity of Magnesium Oxide
$\rho_{\rm s}$	Density of nanofluid
γ	Natural convection parameter
δ	The temporally variable length scale
λ	Porous medium
$\delta_1$	Heat source/sink
Subscript	n
bf	Base fluid
nf	Nanofluid
hnf	Hybrid nanofluid
sp1	AA702
sp2	Zirconium Oxide
sp3	Magnesium Oxide
∞	Ambient condition
w	Condition on surface
Superscript	
,	Differentiation concerning $\eta$
*	Dimensionless properties
	FF

### References

- [1] V.M. Falkneb, S.W. Skan, LXXXV. Solutions of the boundary-layer equations, London, Edinburgh Dublin Phil. Mag. J. Sci. 12 (80) (1931) 865–896.
- [2] W. Ibrahim, A. Tulu, The magnetohydrodynamic (MHD) boundary layer flows past a wedge with heat transfer and viscous effects of nanofluid embedded in porous media, Math. Probl Eng. 2019 (1) (2019) 4507852.
- [3] A. Mishra, M. Kumar, Numerical analysis of MHD nanofluid flows over a wedge, including effects of viscous dissipation and heat generation/absorption, using the Buongiorno model, Heat Transfer 50 (8) (2021) 8453–8474.
  [4] M. Hussain, S. Jahan, Q.A. Ranjha, J. Ahmad, M.K. Jamil, A. Ali, Suction/blowing
- [4] M. Hussain, S. Jahan, Q.A. Ranjha, J. Ahmad, M.K. Jamil, A. Ali, Suction/blowing impact on magneto-hydrodynamic mixed convection flow of Williamson fluid through stretching porous wedge with viscous dissipation and internal heat generation/absorption, Results in Engineering 16 (2022) 100709.
- [5] S.U. Choi, J.A. Eastman, Enhancing Thermal Conductivity of Fluids with Nanoparticles (No. ANL/MSD/CP-84938; CONF-951135-29), Argonne National Lab.(ANL), Argonne, IL (United States), 1995.
- [6] Adnan, W. Ashraf, Thermal efficiency in hybrid (Al2O3-CuO/H2O) and ternary hybrid nanofluids (Al2O3-CuO-Cu/H2O) by considering the novel effects of imposed magnetic field and convective heat condition, Waves Random Complex Media (2022) 1–16.
- [7] M. Bilal, I. Ullah, M.M. Alam, W. Weera, A.M. Galal, Numerical simulations through PCM for the dynamics of thermal enhancement in ternary MHD hybrid nanofluid flow over the plane sheet, cone, and wedge, Symmetry 14 (11) (2022) 2410
- [8] N.A. Zainal, I. Waini, N.S. Khashi'ie, R. Nazar, I. Pop, MHD hybrid nanofluid flow past A stretching/shrinking wedge with heat generation/absorption impact, CFD Lett. 16 (6) (2024) 146–156.

- [9] M. Kezzar, N. Nafir, D.I.B. Amar, M.R. Sari, N. Dwivedi, N.F.M. Noor, I. Tabet, MHD Boundary Layer Flow of Ternary Hybrid Nano-Fluid (Tio2-Sio2,-Al2o3/ H2O-C2h6o2) A Numerical and Analytical Investigations, 2023.
- [10] N. Amar, Viscous dissipation and heat transfer effect on MHD boundary layer flow past a wedge of nano fluid embedded in a porous media, Turkish Journal of Computer and Mathematics Education (TURCOMAT) 12 (4) (2021) 1352–1366.
- [11] R. Ahmad, W.A. Khan, Effect of viscous dissipation and internal heat generation/ absorption on heat transfer flow over a moving wedge with convective boundary condition, Heat Tran. Asian Res. 42 (7) (2013) 589–602.
- [12] R.S. Nath, R.K. Deka, A numerical study on the MHD ternary hybrid nanofluid (Cu-Al2O3-TiO2/H2O) in the presence of thermal stratification and radiation across a vertically stretching cylinder in a porous medium, East European Journal of Physics (1) (2024) 232–242.
- [13] K. Das, P.R. Duari, Effects of nanoparticle shape factor on radiative ternary hybrid nanofluid flow over a wedge in the induced magnetic field, Multidiscip. Model. Mater. Struct. 20 (3) (2024) 486–509.
- [14] H. Berrehal, S. Dinarvand, P. Soni, H. Tamim, MHD radiative Gr-Ag-TiO2/H2O ternary hybrid nanofluid flow upon a permeable movable wedge with irreversibility analysis, Int. J. Model. Simulat. (2024) 1–17.
- [15] M. Shanmugapriya, R. Sundareswaran, P.S. Kumar, G. Rangasamy, Impact of nanoparticle shape in enhancing heat transfer of magnetised ternary hybrid nanofluid, Sustain. Energy Technol. Assessments 53 (2022) 102700.
- [16] Y. Ding, H. Alias, D. Wen, R.A. Williams, Heat transfer of aqueous suspensions of carbon nanotubes (CNT nanofluids), Int. J. Heat Mass Tran. 49 (1–2) (2006) 240–250
- [17] H. Berrehal, A. Maougal, Entropy generation analysis for multi-walled carbon nanotube (MWCNT) suspended nanofluid flow over a wedge with thermal radiation and convective boundary condition, J. Mech. Sci. Technol. 33 (1) (2019) 459–464.
- [18] R. Kandasamy, I. Muhaimin, R. Mohammad, Single-walled carbon nanotubes on MHD unsteady flow over a porous wedge with thermal radiation with variable

- stream conditions, Alex. Eng. J. 55 (1) (2016) 275–285. El-Sayed, E.A., Alwawi, F. A., Aljuaydi, F. and Swalmeh, M.Z., 2024.
- [19] Computational insights into shape effects and heat transport enhancement in MHD-free convection of polar ternary hybrid nanofluid around a radiant sphere. Sci. Rep., 14(1), p.1225.
- [20] A.Z. Ullah, X. Guo, T. Gul, I. Ali, A. Saeed, A.M. Galal, Thin film flow of the ternary hybrid nanofluid over a rotating disk under the influence of magnetic field due to nonlinear convection, J. Magn. Magn Mater. 573 (2023) 170673.
- [21] W.A. Khan, R. Culham, R.U. Haq, Heat transfer analysis of MHD water functionalised carbon nanotube flow over a static/moving wedge, J. Nanomater. 2015 (1) (2015) 934367.
- [22] J.K. Zhang, B.W. Li, H. Dong, X.H. Luo, H. Lin, Analysis of magnetohydrodynamics (MHD) natural convection in 2D and 3D cavity with thermal radiation effects, Int. J. Heat Mass Tran. 112 (2017) 216–223.
- [23] R. Kandasamy, V. Vignesh, A. Kumar, S.H. Hasan, N.M. Isa, Thermal radiation energy due to SWCNTs on MHD nanofluid flow in the presence of seawater/water: Lie group transformation, Ain Shams Eng. J. 9 (4) (2018) 953–963.
- [24] A. Sattar, Unsteady hydromagnetic free convection flows with Hall current mass transfer and variable suction through a porous medium near an infinite vertical porous plate with constant heat flux, Int. J. Energy Res. 18 (9) (1994) 771–775.
- [25] N.G. Kafoussias, N.D. Nanousis, Magnetohydrodynamic laminar boundary-layer flow over a wedge with suction or injection, Can. J. Phys. 75 (10) (1997) 733–745.
- [26] P.V. Murthy, S. Mukherjee, D. Srinivasacharya, P.V. Krishna, Combined radiation and mixed convection from a vertical wall with suction/injection in a non–Darcy porous medium, Acta Mech. 168 (2004) 145–156.
- [27] H. Schlichting, J. Kestin, Boundary Layer Theory, vol. 121, McGraw-Hill, New York, 1961.
- [28] R. Kandasamy, I. Muhaimin, A.K. Rosmila, The performance evaluation of unsteady MHD non-Darcy nanofluid flow over a porous wedge due to renewable (solar) energy, Renew. Energy 64 (2014) 1–9.